2019
January

# Sustainable Marine Structures

# Editorial Board

# SUSTAINABLE MARINE STRUCTURES

Editor-in-Chief

**S. Surendran**
*IIT Madras, India*



NAN YANG ACADEMY OF
SCIENCES (SINGAPORE)

# Contents

## Article

## ARTICLE

# Mechanical Behavior of Patched Steel Panels at Elevated Temperatures

**S Surendran[1]\*   G L Manjunath[2]   S K Lee[3]**

1. Department of Naval Architecture & Ocean Engineering, Indian Institute of Technology Madras, India

2. Research Scholar, Department of Ocean Engineering, Indian Institute of Technology Madras, Chennai, India

3. Pusan National University, South Korea

ABSTRACT

Preventive maintenance is an accepted practice in engineering to keep the structural reliability of ship hulls at the highest possible level. Designers ensure a longer period in between the consecutive maintenance of ship hull parts to optimize expenditure. This is relevant in view of the difficulty in reaching farthest corners in ballast tanks, fuel storage tanks, cofferdams etc. Prior maintenance of the deck and hull parts save a considerable amount of the owner's budget. A portable technology like patching becomes more handy and economic. Performance of both unpatched and patched samples during dynamic loading conditions being examined in the present investigation. The high strength steel panels with a dimension of 70mm×15mm×3mm were edge cracked for lengths of 4mm and 7mm, with width of 1mm for both. The edge cracked high strength steel panels are repaired with composite patches using GFRP (glass fiber reinforced plastic), CFRP (carbon fiber reinforced plastic) and AFRP (aramid fiber reinforced plastic). The patching was done by 3 and 5 layered and impact tested by Charpy impact tester at ranges of high temperatures. The amount of energy absorbed in the impact is converted to dynamic fracture toughness values and compared for evaluating the performance of FRP (fiber reinforced plastics). Finite element analysis was done for evaluating the stress intensity factors at different types of patching and testing conditions. Comparatively the AFRP patched samples showed better dynamic fracture toughness values at different temperatures.

## 1. Introduction

Steel and aluminum are widely used in marine applications. Marine structures constructed using these metals will be subjected to dynamic and fatigue loadings under different environmental conditions. Because of continuous exposure of the structure in marine atmosphere cracks may develop and lead to catastrophic failure of the entire structure. The fracture control in structural components is one of the most important areas which require detailed study. Understanding the characteristics of failures from previous case studies can deepen the knowledge in building a safe and reliable structure. There is always scope for a question of how to increase the materials performance in different operating conditions. The

*\*Corresponding Author:*
*S Surendran,*
*Department of Ocean Engineering, Indian Institute of Technology Madras, Chennai, India.*
*Email: sur@iitm.ac.in*

protection of materials in a marine environment is always a challenge to both to the designer and operator. Two types of approaches are adopted, which are permanent and temporary repair methods. In permanent repair solutions, a designer should accommodate major or minor modification in the design by reinstalling or removing some parts of a structure after the crack confirmation. Temporary repair solutions use traditional industrial practices like re-welding over the crack, riveting or drilling hole near the crack tip for arresting crack growth and grinding off the cracks. These are effective up to a certain extent, but the welding or grinding of soft metals will make it unfit for structural applications. The method composite patching can be done with low cost, ease of portability and ready to use for repairs. The composite patching can be used for repairing micro to macro-cracks. Patching is useful in effective maintenance of decks and other superstructures of ships and offshore structures subjected to different environmental conditions.

The inspiration for the present work is derived from the literature reviews and innovative findings till date. The investigators in the early 70s [5,6] studied the behavior of metals subjected to dynamic loading and different environmental conditions. The designers and analysts understood the importance of mechanical behavior of metals and started studying the characteristics and reasons for failures. A few authors [8,9,12] found it uneconomical in bringing major modifications for the existing structures i.e., permanent modifications. They started suggesting the repair schemes for the existing structures and developed the traditional repairing methods. The traditional methods showed limitations such as time-consuming and sometimes non-effective in arresting the crack growth. Therefore in mid-80s industries shifted to composite materials for repairing structural components. Designers started proposing composites in the fundamental design considerations [7]. The structural components repaired using composite patches showed improvement in duty cycles[10]. Professional bodies like IACS (International Association of Classification Societies) and TSCF (Tanker Structure Co-Operative Forum) recognized composite for repairing of crack as industrial practices [11].

In the early 90s [13,14] industries emphasized improving the quality of repair by considering factors such as the location of the crack, factor for crack growth etc. Many procedures were proposed by ASTM (American Society of Testing Methods) for applicability of the composites in repairing the corroded cracked parts. After patching the cracked metals corroded less and showed an increase in duty cycles. In the late 90s and early 2000s, the corridors of material technology witnessed the use of composite op-timum patch thickness which can have a significant effect on crack trajectories [15,16]. The fiber orientations will help in arresting the mixed mode crack leading to increased reliability.

Even though composites showed promising in repairing of cracked panels, studies showed that care to be taken while production processes. Many researchers pointed out that debonding as the primary reason leading to failures because of rupture with the substrate[18]. Debonding occurs due to the bending of specimens, manufacturing defects or high peel stress near the patched area and the combination of all these. Industries always had a concern towards the application of composites in impact testing because of these limitations. Different types of FRP used showed an impact on the energy absorption capacity of the repaired components [19,20]. The different number of patch layers an influenced improving energy absorption capacity.

The composites showed a limitation to humidity and ultraviolet radiations during their duty cycles. Aging of composites is responsible for the reduction in mechanical properties and may lead to catastrophic failures [21]. Some researchers adopted different types of filler materials and testing procedures for evaluating the performance of composites[22,23]. Finite element analysis was used for analyzing the stress intensity factor at different moisture and temperature conditions. Attention was paid in analyzing the crack growth behavior considering different adhesive properties, a geometry of the patch and its influence on reducing the stress intensity factor[24-26]. An attempt was made recently by testing the samples at low temperatures and it was observed that different types and orientation of fibers in FRPs showed influence on dynamic fracture toughness of the repaired samples[27]. At low temperatures, the patched samples were able to maintain the dynamic fracture toughness values without much variation and that was true even at cryogenic conditions. In one of the mechanical tests, it was observed that the patching could reduce the stress field around the crack[28]. Optimization of mechanical properties and geometric parameters of patches will affect the performance of damaged structures [29].

An attempt has been made in present work to repair structural components of high strength steel. Steel patched samples were tested for high temperatures; energy absorption at the respective temperatures was noted and later converted to dynamic fracture toughness values. The behavior of the composite patched panels at different temperatures along with variation in fracture toughness was observed. Corresponding stress intensity factor values were found for different crack lengths using finite element analysis. This exercise was performed for with and without patches at different temperatures.

## 2. Experimental and Numerical Works

### 2.1 Experimental Details

The Charpy impact test was carried out on the high strength steel patched samples using three different types of composite materials, widely used as structural components. Tables 1 and 2 shows the properties of patch and substrate materials taken for the study. The test piece is a rectangular bar of dimension 70mm×15mm×3mm, with a crack length of 4mm at the center and crack width 1mm. The same test piece with 7mm crack length also used figures 1(a) and 1(b) are relevant to this discussion. The samples were patched by hand layup process using bidirectional GFRP, AFRP and CFRP and later pressure were applied.

Three layers and five layers patches were prepared according to ASTM D2093. After preparing the patches were allowed for 48hrs curing before testing. The dimensions of the patches are 30 mm×10 mm dimensions are considered in such a way that notch is covered completely concerning Khallili et al. [19]. The number of plies is considered based on fracture toughness values from mechanical testing. The stiffness ratio (SR) is calculated based on the equation [19];

$$SR = \frac{E_p t_p}{E_s t_s} \quad (1)$$ Where E is Young's modulus, t is the

thickness, subscript p and s stand for patch and substrate properties. SR ratios of different types of FRPs are shown in table 3.

The patch thicknesses are different for different types of FRPs shown in table 3.Araldite 2015 was used as an epoxy resin for patches of FRPs to the substrate. The area around the notch of a substrate is roughened by scrubbing, for better bonding of FRPs to the metal surface. The bond line thickness is insignificant because just we have applied one layer, and no pressure for bonding was applied, and the patch is double-sided. Figure 1(c) shows the patched crack on the sample. The samples were tested at temperatures of 30℃ , 100℃ , and 250℃ . The samples absorbed a certain amount of energy before it broke and later the influence of temperature  on the dynamic fracture toughness were noted.

For converting the Charpy values (Impact values) to KIc (Fracture toughness) as per Novak-Rolfe ASTM STP 466 (1970)

$$\left(\frac{K_{Ic}}{\sigma_y}\right)^2 = 5\left(\frac{\text{Charpy values}}{\sigma_y - 0.05}\right) \quad (2)$$

Where, fracture toughness $K_{Ic}$ in MPa√m, Charpy values in joules, $\sigma_y$ yield strength of the substrate material in MPa.

Followed by experiment the simulation is done using FRANC 2D/L for plane layered structures. The stress intensity factors for different crack length at different temperatures were simulated using FRANC software.

The equation (2) is used for arriving at the stress intensity values at different crack lengths and comparing with FRANC values for validation.  For single edged notched bend sample, equation as per Anderson [2]

**Table 1.** Mechanical properties of tested materials

| Type of material | Young's modulus E (GPa) | Poisson's ratio υ | Density ρ(g/cc) | Yield strength σy(MPa) | Co-efficient of thermal expansion α ( /℃ ) |
|---|---|---|---|---|---|
| High strength steel | 210 | 0.3 | 7.8 | 353.4 | 11.6×10⁻⁶ |

**Table 2.** Mechanical properties of composite materials

| Type of composite | Young's modulus E₁ (GPA) | Young's modulus E₂ (GPA) | G₁₂ (GPA) | Poisson's ratio υ | α (strain/K) | β (strain/K) | Density ρ(g/cc) | Volume fraction |
|---|---|---|---|---|---|---|---|---|
| GFRP (E- glass) | 25 | 25 | 4 | 0.2 | 11.6 | 0.03 | 1.6 | 0.5 |
| CFRP(300 GSM) | 70 | 70 | 5 | 0.1 | 2.1 | 0.07 | 1.9 | 0.6 |
| AFRP (29) | 30 | 30 | 5 | 0.2 | 7.4 | 0.07 | 1.4 | 0.4 |

**Table 3.** Mechanical properties of tested materials

| Type of FRP | Stiffness ratio of different layers | | Thickness of layers   (in mm) | | Mass of layers   (in gm) | |
|---|---|---|---|---|---|---|
| | 3 layers | 5 layers | 3 layers | 5 layers | 3 layers | 5 layers |
| GFRP | 0.015 | 0.025 | 0.39 | 0.65 | 0.245 | 0.4017 |
| CFRP | 0.0566 | 0.094 | 0.51 | 0.85 | 0.244 | 0.408 |
| AFRP | 0.0165 | 0.0273 | 0.345 | 0.575 | 0.1449 | 0.2415 |

$$K_I = \frac{P}{B\sqrt{W}} f\left(\frac{a}{w}\right) \qquad (3)$$

$$f\left(\frac{a}{w}\right) = \frac{3\frac{s}{w}\sqrt{\frac{a}{w}}}{2\left(1+2\frac{a}{w}\right)\left(1-\frac{a}{w}\right)^{\frac{3}{2}}}\left[1.99 - \frac{a}{w}\left(1-\frac{a}{w}\right)\left\{2.15 - 3.93\left(\frac{a}{w}\right) + 2.7\left(\frac{a}{w}\right)^2\right\}\right]$$

Where $K_I$ is a stress intensity factor, and w length and width of crack, B breadth, P load, S length of the sample, f(a/w) correction factor.
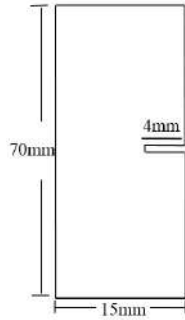


**Figure 1.** (a) 4mm cracked panel
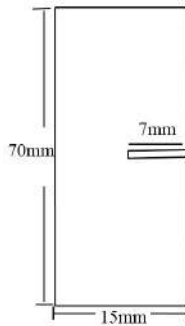


**Figure 1.** (b) 7mm cracked panel.
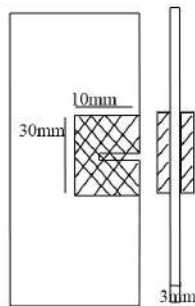


**Figure 1.** (c) Patch dimensions

Figure 1(a) and 1 (b) illustrates the dimensions of cracked panels prepared as per ASTM D 2093 and in figure 1 (c) shows the patch dimensions along with thickness.

Figure 1 (d) consists of patched and unpatched samples before testing or after testing which is destructive.

Figure 1(e) shows the description of the testing device, the samples after patching are mechanically tested. The samples are placed on the sample holder, and the pendulum hits the sample shown in figure 1(f). The energy absorbed by the sample is indicated by the device. The notched sample is kept with the crack tip facing the pendulum, and corresponding reading are noted.
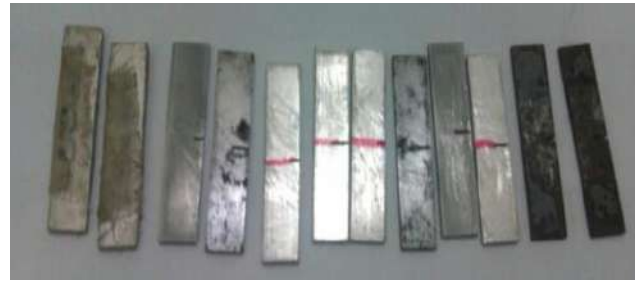


**Figure 1.** (d) Patched and unpatched samples



**Figure 1.** (e) Charpy impact tester
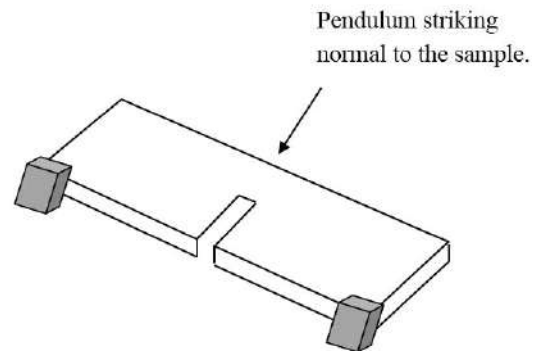


**Figure 1.** (f) Position of sample

**Figure 1.** (g) Samples after the tests



**Figure 1.** (h) Samples exposed to a temperature of 250℃ beyond

The figures1 (d) and 1 (g)illustrates the patched and unpatched samples which were tested at different temperatures. Only 5 layered AFRP found bending and observed the right amount of energy compared to 3 and 5 layered GFRP and CFRP and even 3 layered AFRPpatched samples. The unidirectional laminates with different layers are obstructing the growth of the crack. The patching is effective in closing the width of the crack and lessens the stress at the crack tip and further growth of crack is stopped. Debonding is one of the major problems during tests and normally starts from the edges. Care is to be taken during manufacture as the debonding can lead to failure of a sample with less energy absorbed. The samples tested at different temperatures were able to retain the fracture toughness values at certain temperatures. Even after exposing to high temperature, a slight change in color of the patch is observed without affecting the fracture toughness of the sample. But up to 250℃ , the patched samples retained their strength and beyond this temperature, patches lost their original appearance that is derivated from figure 1 (h). Five layers AFRP patched samples are found bent as a result of fibers crossing each fiber, while other patched samples failed by fiber pullouts.

## 2.2 Simulation Details

The modeling is done by CASCA for initial meshing, the input for FRANC 2D/L is created. The input file is fed into FRANC software for estimating the stress intensity factors for different crack lengths. The material properties, boundary conditions, and analysis typesetting can be performed by FRANC software. The winged edge data structure is used in the design and analyses of FRANC 2D/L software. The winged data structure consists of vertices, faces and edges have main entities. These entities represent finite nodes and elements, the data structure contains adjacency information. This reduces the time required for finite element analysis and the adjacency defines the structural boundaries. Adjacency helps in deleting the elements during the crack propagation without deleting the edges and helps in recomputing the stiffness matrices. The software uses eight and six node elements with quadratic shape function by performing an elastic analysis. The stress singularity near the crack tips can be computed by moving six nodes to the quarter point locations. During analyzing coated samples the interface elements have relied upon to represent contact between surfaces. A relationship for defining the surface tractions are integrated for nodal loads during the dynamic relaxation solution. The linear elastic fracture analysis concepts are used for calculating stress intensity factors using displacement correlation or modified crack closure methods. During the crack propagation, the automatic remeshing strategy is adapted to delete the elements vicinity of the crack tip. Move the crack tip and then insert the trial mesh for connecting to the new crack of existing mesh. The dynamic relaxation solver is performed for damping solution until all the motion stops. During each iteration, the external load vector is calculated and the matrix multiplication is performed and subtracted along with the damping terms. As the acceleration and velocity terms approach zero, static equilibrium is achieved by balancing internal forces and external ones. The solution scheme is stable and will converge after many iterations depending on eigenvalues.

## 3. Results and Discussions
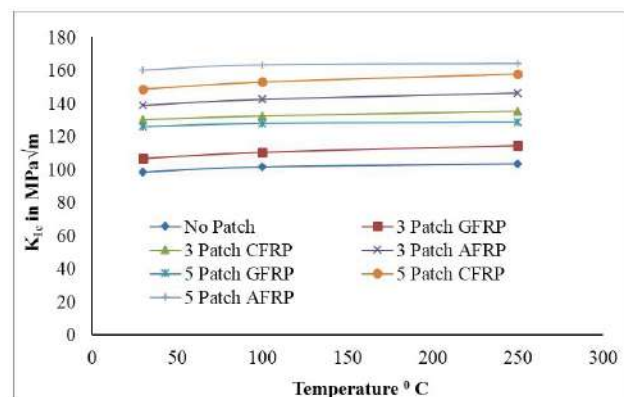


**Figure 2.** 4mm cracked panels fracture toughness against temperature

Figure 2 illustrates the fracture toughness of the 4mm cracked panels with and without a patch for different numbers of layers, types of patches at different temperatures. The variation in fracture toughness is observed for different types of patches. The fracture toughness is constant for particular patching.
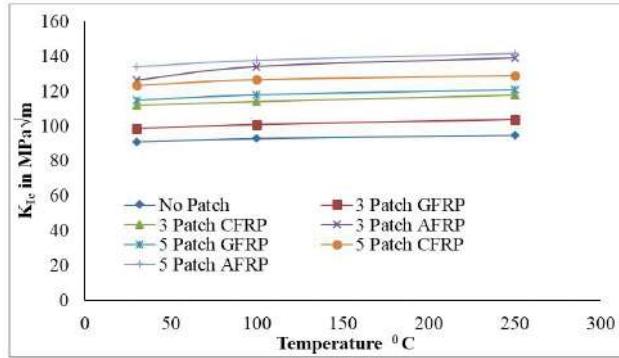


**Figure 3.** 7mm cracked panels fracture toughness against temperature

The observation for fracture toughness for the 7mm cracked panel is shown in figure 3 the trend of variation is similar to that in figure 2. However, there is a difference in fracture toughness values. Due to an increase in crack length value of 7mm the patch dimensions are unchanged therefore a decrease in toughness values. At a certain temperature, the fracture toughness of the patched samples was maintained without much difference, beyond which the fracture toughness decreased drastically. However, fire element retardant ingredients can be added to the composite so that the patching will maintain the mechanical properties like fracture toughness at higher temperatures.
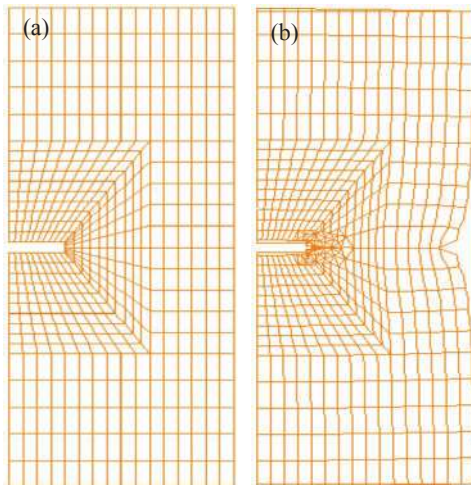


**Figure 4.** (a) Sample before cracking

**Figure 4.** (b) Initiation of crack
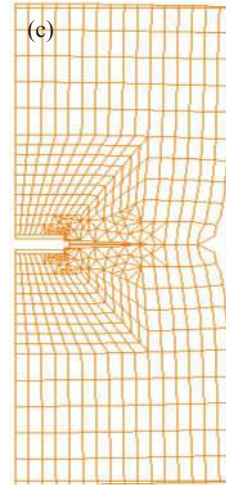


**Figure 4.** (c) Propagation of crack

Figure 4(a) illustrates unpatched samples before cracking and figures 4(b) shows its initiation. Figure 4(c) shows the propagation of the crack.

Figure 4(d) illustrates the fully grown crack along with the sample deformation because of no resistance for the crack growth and sample fails. Simulation of patched samples shows increment in energy absorption and obstruction for the growth of crack compared to unpatched samples illustrated in figure 4(e). Figure 4(f) shows the remeshing in the patched sample along with crack growth. The patching along with a number of layers is having an impact on the crack growth and reduced stress intensity near crack tip.
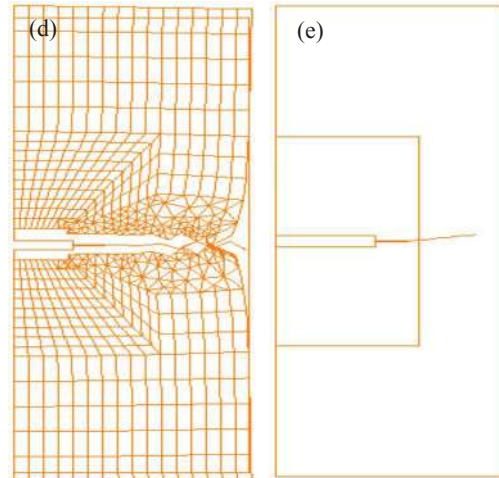


**Figure 4.** (d) Fully developed crack

**Figure 4.** (e) Patched sample along with crack

The validation of stress intensity factor between analytic values as per equation (2) and FRANC 2D/Lare shown in figures 5(a) and 5(b) for 4mm and 7mm cracked panels respectively. The analytical and FRANC values are calculated for different crack lengths and compared, a good

agreement can be observed.

The FRANC 2D/L analysis for different crack lengths and temperatures are shown in the following figures. Steel patched samples tested at high temperature shows an increase in $K_I$ values for unpatched compared to patched ones. The $K_I$ values vary for different types and layers of patched samples.
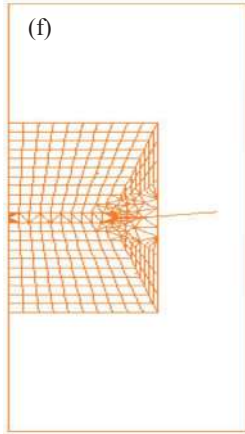


**Figure 4.** (f) Patched sample with further crack growth
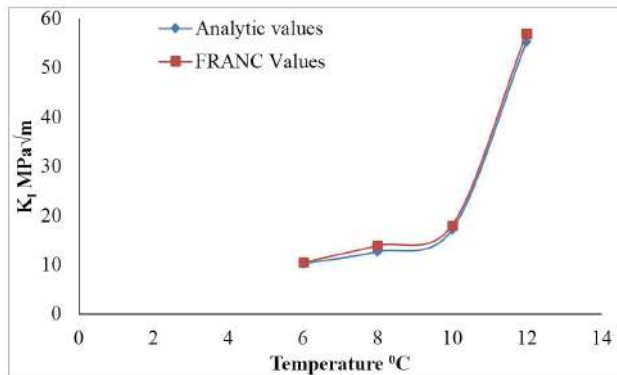


**Figure 5.** (a) Comparison of stress intensity factor for 4mm cracked panels
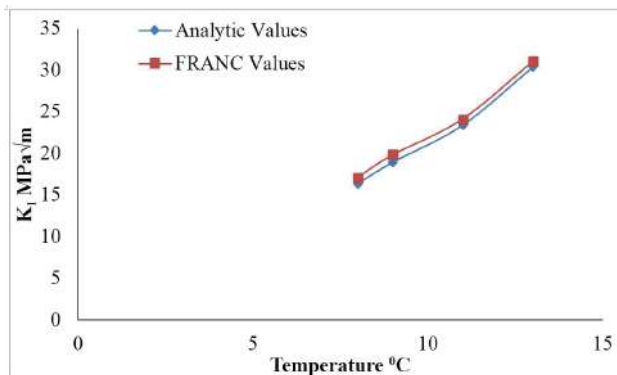


**Figure 5.** (b) Comparison of stress intensity factor for 7mm cracked panels
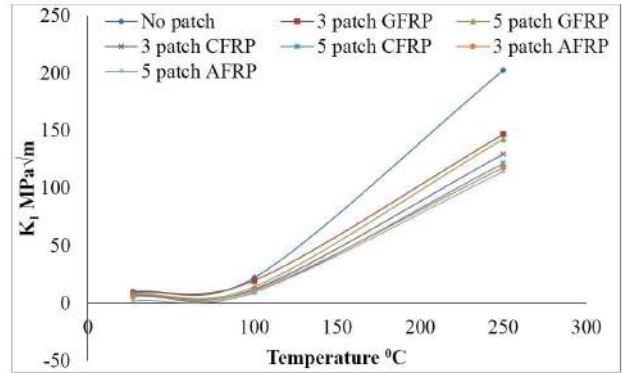


**Figure 6.** I against temperature for an increase in crack length from 4mm to 6mm

Comparatively the increase in patch layers shows a decrement in $K_I$ values, offering obstruction for crack bridging.
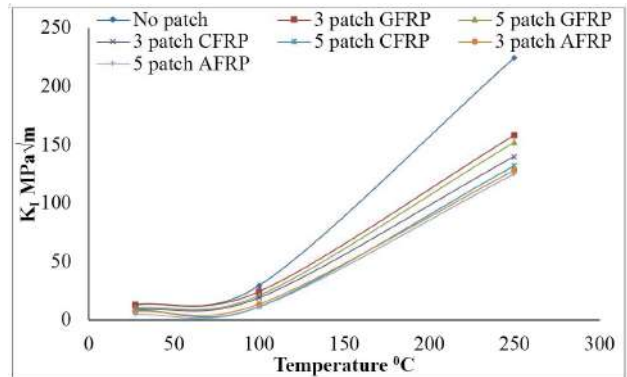


**Figure 7.** $K_I$ against temperature for an increase in crack length from 4mm to 8mm

Further in figure 7 the increment in crack length made KI rise in value and variation is similar to figure 6 with high $K_I$ values. As per figure 8, the crack neared the end of patch boundary leading to a sudden increase in $K_I$ value. The dimension of patching has an influence on the $K_I$ values and as the crack near the end of patch, area showed a striking effect on crack bridging phenomenon.
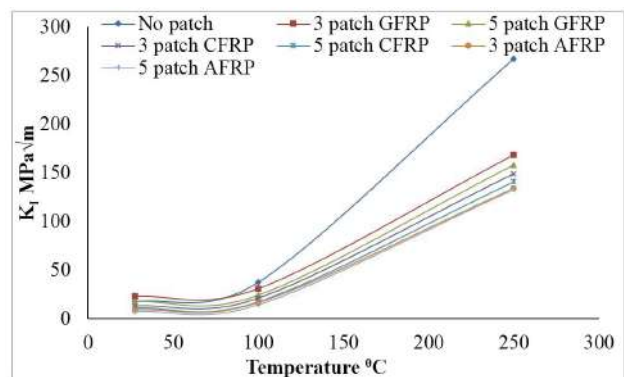


**Figure 8.** $K_I$ against temperature for an increase in crack length from 4mm to 10mm

Therefore the crack bridging is occurring easily without much obstruction for crack growth.
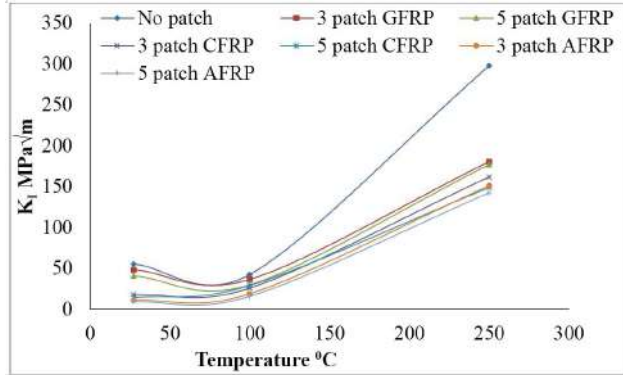


**Figure 9.** $K_I$ Against temperature for increase in crack length from 4mm to 12mm

The crack after crossing the patched area shooting up in stress intensity factor can be seen in figure 9. In patched sample the crack after crossing the patched area there is a small variation in stress intensity values. Except in 5 layered patch there is an increase in fracture toughness and reduced stress intensity values. The increase in patching layers has shown a promise in case of repairing macrocracks.

In 7mm cracked steel patched samples a further increase in $K_I$ value is seen in figure 10. With increase in crack length and keeping patch dimensions same, there is an increase in stress intensity values fro 7mm cracks. The variation in patch dimensions can influence the crack growth resistance.
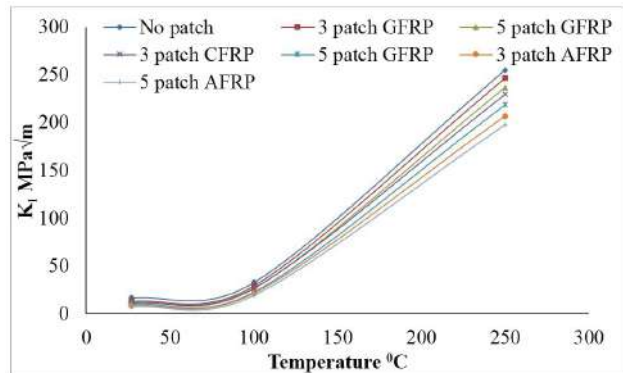


**Figure 10.** $K_I$ Against temperature for an increase in crack length from 7mm to 8mm

In 7mm cracked panels an increase in stress intensity values can be observed as predicted and this is in comparison with 4mm cracked panels in figure 10. The crack length increment in the patched sample there will be minimal effect on stress intensity values.
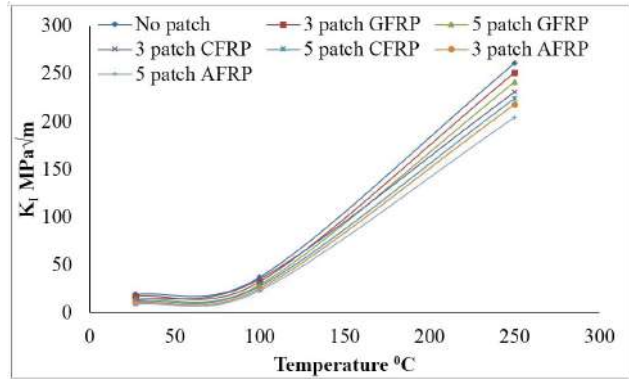


**Figure 11.** $K_I$ Against temperature for an increase in crack length from 7mm to 9mm

There was a relative difference in growth in $K_I$ value as the crack neared the patch boundary and it is shown in figure 11. Again the increase in crack length reduced the stress intensity value difference in unpatched and patched conditions. The increase in a number of patch layers has a minimal effect on the fracture behavior and stress intensity values.
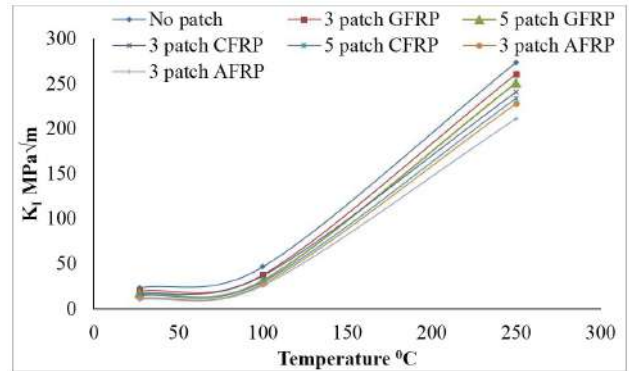


**Figure 12.** $K_I$ Against temperature for an increase in crack length from 7mm to 11mm

Figure 12 and 13 shows the $K_I$ values at a higher temperature for longer crack length. At lower temperature, its is non-linear and at high temperature say 100℃ it is almost linear.
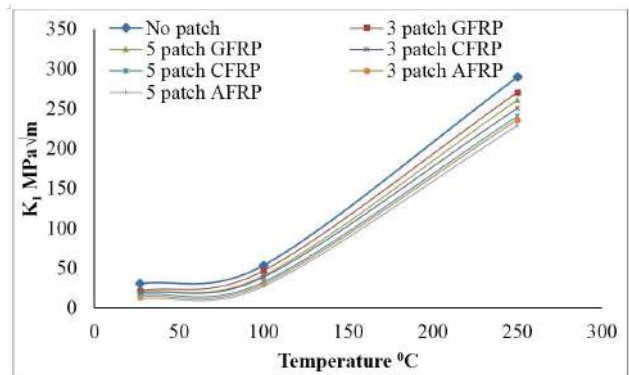


**Figure 13.** $K_I$ Against temperature for an increase in crack length from 7mm to13mm

The non-linear increase in the value of stress intensity against temperature is observed. However, the patches are ineffective at such high temperatures. Therefore the dimensions of patch play a key role in arresting or offering a resistances for the crack to grow. The AFRP patched samples at high temperatures were able to increase in DFT values compared to GFRP, and CFRP patched samples. Experimental investigation along with simulation showed the influence of temperature on the dynamic fracture toughness of the patched samples. The 5 layeredAFRP patched samples were found to bend and absorb a good amount of energy. The crack bridging is not occurring effectively in 5 layered AFRP samples compared to other patched samples. The crack tip is getting blunted after crossing each fiber in 5 layered AFRP; in other samples, this phenomenon cannot be observed. The energy required for crack propagation is observed by fibers in the case of 5 layered AFRP patches; while the other patched samples are broken by fiber pullouts. The temperature is playing an important role in ductility transition of the patched samples. Unidirectional composite patches exhibited superior properties at different temperatures when compared to bidirectional composites. The patched samples depending on a number of layers are able to withstand for certain temperatures. At say 30℃ and 100℃ with sample showing a gradual loss in the fracture toughness of patched samples. While at 250℃ a sudden reduction in effectiveness can be observed. From the trend of figure 13 it can be inferred that a temperature of roughly 175℃ is the safe limit for the patches to be relied upon. There is always a scope for arriving at an optimum patch area at different crack lengths.

## 4. Summary and Conclusions

The high strength steel samples were cut to 70mm×15mm×3mm, edged crack of 4mm and 7mm at the centre. The 3 and 5 layers patching was done using GFRP, CFRP and AFRP and impact tested by Charpy for evaluating dynamic fracture toughness values. The application of composite patch for repairing crack is found regarding the crack growth and stress intensity factor. Therefore increases the life of the structure to perform well in certain demanding condition to overcome the challenges. The performance of composites in different temperatures and environmental conditions still remains as a challenge; an attempt is to reconfirm the effectiveness of composites at high temperatures. The following conclusions are arrived at:

※As the temperature of marine hulls is near to the medium in which it floats, the technology is found suitable. If the temperature is high say 250℃ , due to some reasons, the patches are found ineffective.

※The 5 layered AFRP patches proved excellent compared to other types and layers of patches because of more energy absorption.

※While characterizing the fractured samples it was observed that in 3-layered and 5-layered patched samples of GFRP, CFRP and only 3-layered AFRP samples cracked by fiber pullout.

※The 5-layered AFRP were found bending leading to de-bonding of patches but no fiber pullouts beyond 3- the layer of the patch.

※AFRP can be used effectively in repairing of macro-cracks compared to other types of composite patches.

※The stress intensity factor of crack found drastically increasing after crossing patched area compared to crack inside repaired area using patch.

※The patch dimensions will have an influence on the arresting or resistance for crack.

※The behavior of crack inside and outside the patch area along with stress intensity factor is measured at elevated temperatures by finite element analysis using FRANC 2D/L.

※Selection of filler materials can really influence the performance of FRPs particularly at high temperature applications.

## References

[ 1 ]  Anderson T L. Fracture mechanics fundamentals and its application, CRC Press; 1995.

[ 2 ]  ASTM D 2093, Standard practice for preparation of surfaces of plastics prior to adhesive bonding. In: Annual book of American society for testing materials, 2001, 15(6).

[ 3 ]  Barsom J M, Rolfe S T, 1970. Correlation between K1C Charpy notch test results in the transition temperature range. ASTM STP 466, 1970, 281–302.

[ 4 ]  Wawrzynek P, Ingraffea A. http://www.cfg.cornell.edu/software/Current%20Docs/F2D_V3.1.pdf.

[ 5 ] Hahn G T, Hoagland R G, Kanninen M F, Rosenfield A R and Sejnoha R.Fast fracture resistance and crack arrest in structural steels, by Battelle Memorial Institute under Department of the Navy Naval Ship Engineering Center Contract No. NOO024-72-C-5142.SSC-242, 1973.

[ 6 ] Hahn G T, Hoagland R G, and Rosenfield A R. Dynamic crack propagation and arrest in structural steel, by Battelle Memorial Institute under Department of the Navy Naval Ship Engineering Center Contract No. NOO024-72-C-5142.SSC-256, 1976.

[ 7 ] Eric Greene. Marine Composites investigation of fiberglass reinforced plastics in marine structures, Distribution available from National Technical Information Service, Springfield, VA 22161(703) 487-4650.SSC-360, 1990.

[ 8 ] Gallion K A. Structural Maintenance Project Volume 3, Distribution available from National Technical Information Service, Springfield, VA 22161 (703) 487-4650. SSC-386, 1992.

[ 9 ] Grubbs, Kim and Zanis, Charles. Underwater Repair Procedures for Ship Hulls (Fatigue and Ductility of Underwater Wet Welds), Distribution available from National Technical Information Service, Springfield, VA 22161 (703) 487-4650.SSC-370, 1993.

[10] Dale G. Karr and Anthony Waas (SSC-1469, 2007), Strength and Fatigue Testing of Composite Patches for Ship Plating Fracture Repair, Distribution available from National Technical Information Service, Springfield, VA 22161 (703) 487-4650.

[11] Ge (George) Wang, ABS Corporate Technology. Criteria for Determining Fracture Repair Procedures, Distribution available from National Technical Information Service, Springfield, VA 22161 (703) 487-4650.SSC-SR 1459, 2011.

[12] Baker AA. Repair of cracked or defective metallic components with advanced fiber composites an overview of Australian work. Composite Structure，1984,2,153–81.

[13] Baker AA, Jones R Bonded repair of aircraft structures, Kluwer Academic Publishers; 1988.

[14] Baker AA. Bonded composite repair for fatigue-cracked primary aircraft structure. Composite Structure,1999,74,431–43.

[15] Hosseini-Toudeshky H, Mohammadi B, and Daghyani H R. Mixed-mode fracture analysis of aluminum repaired panels using composite patches. Composite Science Technology, 2006, 66,188–98.

[16] Hosseini-Toudeshky H, Sadeghi G, and Daghyani H R. Experimental fatigue crack growth and crack-front shape analysis of asymmetric repaired aluminum panels with glass/epoxy composite patches. Composite Structure, 2005, 71,401–6.

[17] Xiong J J and Shenoi R A. Integrated experimental screening of bonded composites patch repair schemes to notched aluminum-alloy panels based on static and fatigue strength concepts. Composite Structure , 2008, 83, 266–72.

[18] Nicholas G. Tsouvalis, Lazarus S. Mirisiotisand Dimitris N. Dimou. Experimental and numerical study of the fatigue behavior of composite patch reinforced cracked steel plates. International Journal of Fatigue,2009, 31,1613–1627.

[19] Khalili S M R, Ghadjar R, Sadeghinia M and Mittal R K. An experimental study on the Charpy impact response of cracked aluminum plates repaired with GFRP or CFRP composite patches. Composite Structures ,2009, 89, 270–274.

[20] Khalili, S M R, M Shiravi and A S Noorani. Mechanical behavior of notched plate repaired with polymer composite and smart patches-experimental study. Journal of Reinforced Plastics and Composites 29.19 (2010): 3021-3037.

[21] Emin Ergun, Süleyman Tasgetiren and Muzaffer Topçu-Fatigue and fracture analysis of an aluminum plate with composite patches under the hygrothermal effect. Composite Structures, 2010, 92, 2622–2631.

[22] Megueni.A, Tounsi A, Bachir Bouiadjra B and Serie B. The effect of a bonded hygrothermal aged composite patch on the stress intensity factor for repairing cracked metallic structures. Composite Structures, 2003, 62,171–176.

[23] Megueni. A Tounsi A and Bedia E. Evolution of the stress intensity factor for patched crack with a bonded hygrothermal aged composite repair. Materials and Design, 2007, 28, 287–293.

[24] Ouinas D, Sahnoune M, Benderdouche N and Bachir Bouiadjra B. Stress intensity factor analysis for notched cracked structure repaired by composite patching. Materials and Design, 2009, 30, 2302–2308.

[25] Ouinas D, Bachir Bouiadjra B, Houri S, Benderdouche N. Progressive edge cracked aluminum plate repaired with an adhesively bonded composite patch under full-width disbond. Composites: Part B, 2012,43, 805–811.

[26] Reagan L, Bachir Bouiadjra B,  Belhouari M, Madani K, Server B, and Feaugas X. Effect of composite hygrothermal aging on the SIF variation in bonded composite repair of aircraft structures. Journal of Reinforced Plastics and Composites,2010, 29 (24), 3631–3636.

[27] Manjunath G L and Surendran S. Dynamic fracture toughness of aluminum 6063 with multi-layered composite patching at lower temperatures. Ships and Offshore Structures ,2013, 8(2), 163-175.

[28] Pereira J M, GhasemnejadH, Wen J X, Tam V H Y. Blast response of cracked steel box structures repaired with carbon fiber-reinforced polymer composite patch. Materials &Design,2011, 32(5), 3092-3098.

[29] Ouinas D, Achour B, B BBouiadjra, Taghezout N. The optimization thickness of single/double composite patch on the stress intensity factor reduction. Journal of Reinforced Plastics and Composites , 2013, 32(9), 654-663.

## ARTICLE

# Application Of Fuzzy-Logic In Ship Manoeuvring In Confined Waters

## S. Surendran[1]* and S.K Lee[2]

1. Department of Ocean Engg., Indian Institute of Technology IIT Madras, Chennai 600 036, India

2. Department of Naval Architecture and Ocean engineering, Pusan National University, S Korea

ARTICLE INFO

ABSTRACT

A ship manoeuvring problem is solved using an algorithm built on fuzzy logic. The manoeuvring model for a design ship is coded in C++ and the results are presented here. A bulk carrier is assumed as design ship for a newly setting up harbor along the east coast of India. The harbor mouth is 25 km away from the deep water zone. The approach channel is straight along the 22 km length. Laterally restricted and shallow waters are considered and their influences on hydrodynamic derivatives are discussed. Some sample problems are solved. Trajectories, ship heading, rudder angle, velocities and accelerations, of the moving vessel, are calculated and presented for clarity. The developed code is robust in the sense that any designer or user can easily interact with various input parameters to verify the outputs and their suitability for the design ship meant for a particular water front location. The results are validated using another algorithm built on PID which is discussed in brief.

## 1. Introduction

Along the east coast of India a few marine infrastructure related projects are coming up at present and they are in various stages of completion. New ports and harbours, container terminal etc. are badly needed for the infrastructure starved country for its economic growth. Detailed study on environmental effects and bathymetry surveys is needed to locate a port facility preferably not very far from the deep sea. Internet is become a blessing for fast downloading of maps and topography of any geographical locations. Availability of numerical models save plenty of time for designers to fix the basic parameters and the design ship-waterway compatibility is assured by such numerical models. This paper deals with a ship manoeuvring model in C++ environment which is easy to handle.

Ship manoeuvring deals with the motion of the ship controlled by the ship's operator by activating control surfaces. The helmsman takes measures to reduce the deviation of the actual path of the ship from the required one. In the open sea, the ship's captain has plenty of time and space to monitor and control the direction and speed of the ship. There are control loops for both path or direction and speed. But in restricted waters like approach channels and canals, decisions must be made fast to maintain the clearances within the tolerance from stationary or moving bodies around. The master needs to take steps for collision avoidance ensuring safety. Such a requirement

*Corresponding Author:*

S. Surendran

*Department of Ocean Engg., Indian Institute of Technology IIT Madras, Chennai 600 036, India*

*E-mail sur@iitm.ac.in*

necessitates automation and integration of both the control loops. Path keeping, path changing and speed changing is achieved using the above mentioned control loops.

## 2. Problem Definition

During the design stage, the Naval Architect or the designer can influence the response of the ship with the rudder deflection. The design is done based on deep water performance of the vessel. The hydrodynamic derivatives of the vessel are calculated (Lewis, 1989) and controllability parameters are established. The principal particulars of the vessel and sectional details are relied upon to get such hydrodynamic derivatives. Models are available for both linear and non-linear manoeuvring [1] of surface ships. Similar governing equations were incorporated in the paper on steering characteristics of ships in calm water and waves [2]. Maneuvering criteria of hull using linear theory and correction scheme for the shallow waters were also proposed[3]. Calculation method of ship manoeuvring characteristics at the design stage[4] is also found relevant. A more powerful resource is on models of marine vehicle kinematics and dynamics in 6 degrees of freedom [5]. Mathematical models [6] can be relied upon to solve ship motion and manoeuvring problems to get faster results. Added mass of the moving body in confined waters is an essential component in the governing equations and a procedure is available for computing reasonably accurate values [7].

The application of fuzzy logic, on ship motion and manoeuvring, already becomes an accepted practice among the researchers. Fuzzy logic controller to govern the motions of fins in order to reduce the roll motions of ships was proposed [8] in the past. Comparisons of algorithm on ship manoeuvring and harbor entry were successfully shown [9] for a standard ship of academic interest [5] .A handbook of marine craft and hydrodynamics and motion control, which deal with hydrodynamics modeling and control system [10] is an authentic resource for designers and analysts. An optimized path is preferred to in the approach channel leading to a new port and harbor project [11]. Different international standard and recommendations (Thoresen, 2003) for various design and construction is guidelines towards the minimum clearances around the moving hulls in approach channels.

For a newly planned port and harbor, the length of approach channel, its orientation and other parameters are based on a detailed bathymetry survey for a single design ship or more occupying the berths in the harbor at any point of time [12]. The infrastructure is developed for biggest size vessel. Stopping distance has a bearing on the harbor dimensions, since the ship enters at a low speed and takes a turn nearing its berth [13]. Two loading conditions of the vessel are to be considered. One is for fully loaded arrival or departure and the other for ballast condition. The harbor entrance width is also optimized to minimize the environmental effects inside the harbor. But that requires additional attention and effort of the captain to take the ship through the harbor mouth amidst the possible cross flow of environmental disturbance, especially during monsoon. A breakwater sometimes serves as a multi-purpose platform. Concrete structures like breakwaters extend their foundation into the harbor space thus creating more confinement. As per the continuity equation of fluid dynamics, the reduced area creates more velocity of the particles for the same discharge or mass flow. Analyst of ship manoeuvring should take into account the space reduction due to various protrusions of foundations of marine structures and structure like pillars, plies etc.

### 2.1 Design Ship and Approach Channel

A hypothetical harbor is considered here with an approach channel, a length of 22 km and remaining length start from a curvature along the approach channel and ends up in the harbor entrance. It is presumed that some bathymetry study done by a responsible agency, is available for the project. The design vessel dimensions are given in Table 1.

**Table 1.** Design ship dimensions

| Type of vessel | LOA(m) | LBP(m) | Beam(m) | Draft(m) |
|---|---|---|---|---|
| Bulk Carrier (Coal/Iron Ore) | 250 | 240 | 43.4 | 15.0 |

In this particular case, the approach channel is given as 25 km away from the harbour entry. A cross section of the approach channel is shown in Figure 1 which shows a single lane channel.

After fixing a water depth with sufficient under keel clearance, lateral clearance for the length of the approach channel, a study on various operating conditions of the vessel is taken up. For the approach channel the clearance in the bottom is 20% of the fully loaded draft and that of the inside harbor is 10%. Figures 1 and 2 can be taken as based on a thumb rule for dimensions of the design ship and the approach channel. The width across the curved path is increased by 20% of the normal width of the channel. Normal width of the channel is expressed as a function of the breadth of the vessel. In the above discussions, the requirement of dredging and minimizing the same is very important since the expense of dredging consumes the maximum amount of a new project. The project is planned resulting in least dredging and the expense on the annual maintenance dredging is also is to be minimized. Please also note that transportation and dumping of dredged material is another liability. Minimizing

the use of cutter suction dredger in rocky areas should be born in mind. Use of cutter suction dredger in rocky area is very expensive compared to soft sand cutting. Figure 1 shows the available water depth in un-dredged condition. It also shows how much is intended to be dredged. The dredged slopes are 1/3 – 1/5 and it is decided by the angle of repose of that particular soil to ensure stability of the trench. Under keel clearance is to be ensured and it is to be subjected to the maximum value of the squat. The dredging tolerance is not shown, but a suitable value is to be provided there too. Tide levels are shown in Figure 1 and siltation buffer, allowance for survey inaccuracy etc. are avoided to make the figure look simple and clear.

Along the radius, the width is to be increased as per PI-ANC (Permanent International Association of Navigation Congress) or similar codes. The outer, mean curvature line and inner radius are to be provided and they are given as R1, R2 and R3 respectively. Relevant radii are shown in Figure 2. Actual figures can be arrived at based on standard manuals of PIANC, US Navy publication, BS Codes (Code 6349-4, 1994), Indian standards etc. The width is increased as per a suitable slope along the stretch of the length. The additional width is 40 meters at the middle of the curvature or turn and this higher width is as per norms of international bodies.
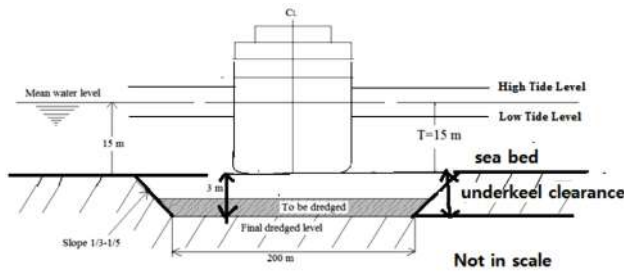


**Figure 1.** One lane channel as per IS - 4651 part (v)
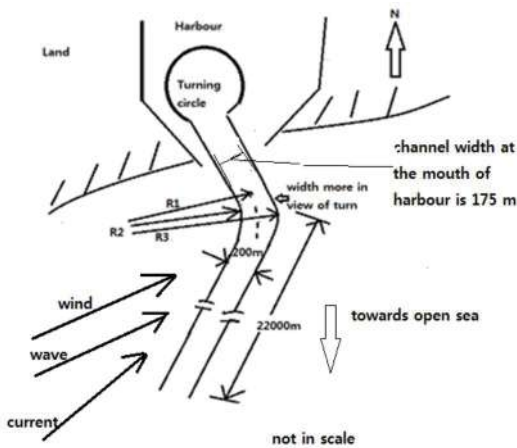


**Figure 2.** Port layout showing curvature and its wider part

The vessel response, if any, to a disturbance in a low speed entry in the approach channel is to be investigated. There are many critical situations in a wavy and windy environmental condition. At the entry point of the harbour, where the width is just 175 m. The ship can sway or yaw or move in a combined mode during cross flows in monsoons and rough weather. In many Indian harbours the entrance width becomes critical during rough seasons. Port of Mangalore and Kandla are examples. The surge, sway and yaw motions are determined using a manoeuvring model developed in connection with this work. The latter two are interlinked or coupled.

## 3. Manoeuvring Model

Two different axes are required to completely specify the motion of a ship. The position of the centre of gravity of the ship is determined in reference to an earth fixed co-ordinate system. The other is the body fixed axis which is fixed on the ship. The x-direction of the body fixed system coincides with the centerline of the vessel and is positive forward. The y-axis runs across the ship in the transverse direction. The z-axis is directed vertically downwards. The angle made by the earth made by the body fixed x-axis with the earth fixed x- axis is called the yaw angle. The resultant velocity vector could make an angle with the body fixed angle and is called drift angle which is non-zero normally. Figure 3 shows the details.
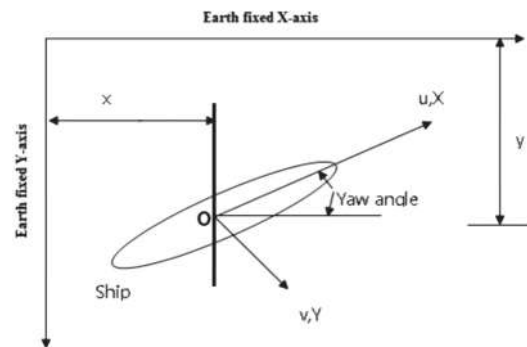


**Figure 3.** Earth fixed axis and body fixed axis system coordinates

As per Figure 3 the forces and moments based on the global earth fixed axes system can be written for the surface ship as follows.

$$X_0 = m\ddot{x}_0 \tag{1a}$$
$$Y_0 = m(\ddot{y}_0) \tag{1b}$$
$$N = I_z\ddot{\psi} \tag{1c}$$

The above equation follows the Newton's law stating that force is equal to the product of mass and acceleration. The subscript 'o' indicates that the values are with respect to the global earth fixed axis. However, the equations are more conveniently expressed when written with respect to

the body fixed axis as follows.

$$X = X_0 \cos\Psi + Y_0 \sin\Psi \tag{2a}$$

$$Y = Y_0 \cos\psi + X_0 \sin\psi \tag{2b}$$

Similarly the velocity components can be written as

$$(\dot{x}_0) = u \cos\psi - v \sin\psi \tag{3a}$$

$$(\dot{y}_0) = u \sin\psi + v \cos\psi \tag{3b}$$

The acceleration terms can be written by differentiating the above equations.

$$(\ddot{x}_0) = \dot{u} \cos\psi - \dot{v} \sin\psi - (u \sin\psi + v \cos\psi)\,\dot\psi \tag{4a}$$

$$(\ddot{y}_0) = \dot{u} \cos\psi + \dot{v} \cos\psi + (u \cos\psi - v \sin\psi)\,\dot\psi \tag{4b}$$

Substituting Eq. (4) in Eq. (1) the governing equations of motions for horizontal plane can be achieved.

$$X = m(\dot{u} - v\psi) \tag{5a}$$

$$Y = m(\dot{v} - u\psi) \tag{5b}$$

$$N = I_z\,\ddot\psi \tag{5c}$$

While deriving the above equations it is assumed that origin O of the body fixed coordinate system is at the centre of gravity G of the vessel. Simplifications are possible if the origin O were chosen at the axis of symmetry. If the newly chosen O is now located at a vector $R_G$ from G, then the above equations become as shown below.

$$X = m(\dot{u} - \dot\psi\,v - y_G\,\ddot\psi - x_G\,\dot\psi^{\,2}) \tag{6a}$$

$$Y = m(\dot{u} - \dot\psi\,v - y_G\,\ddot\psi - x_G\,\dot\psi^{\,2}) \tag{6b}$$

$$N = I_z\,\ddot\psi + m\{x_G(\dot{v} + u\dot\psi)\} \tag{6c}$$

If the ship is symmetric with respect to the centerline $y_G$ can be neglected, ie. when $y_G$ is equal to zero the above equations become as follows.

$$X = m(\dot{u} - \dot\psi v - x_G\dot\psi^2) \tag{7a}$$

$$Y = m(\dot{v} + u\Psi + x_G\Psi^2) \tag{7b}$$

$$N = I_z\ddot\psi + mx_G(\dot{v} + u\dot\psi) \tag{7c}$$

The Eq. (7) show coupling between surge and sway velocities and yaw rate. These equations lead to a simpler set of equations for linear case as follows.

$$X = m\dot{u} \tag{8a}$$

$$Y = m(\dot{v} + u\dot\psi + x_G\ddot\psi) \tag{8b}$$

$$N = I_z\ddot\psi + mx_G(\dot{v} + u\dot\psi) \tag{8c}$$

Eq. (8 a) is called the linear speed equation and Eq. (8 b) and (8 c) are called the steering equations. Eq. (8 a) is independent and the other two are mutually coupled. A good numerical approach is sufficient for the solution of these equations. It can be assumed that X, Y and N are functions of various velocities and accelerations in connection with the motion of the hull. Therefore, X, Y and N can be written as follows.

$$X = F_x(u, v, r, \dot{u}, \dot{v}, \dot{r}) \tag{9a}$$

$$Y = F_y(u, v, r, \dot{u}, \dot{v}, \dot{r}) \tag{9b}$$

$$N = F_\psi(u, v, r, \dot{u}, \dot{v}, \dot{r}) \tag{9c}$$

Assuming an equilibrium condition and applying Taylor's series expansion the non-dimensional form of the steering equations as per the practices in maneuvering studies is reduced to the following equations.

$$-Y_v'\,v' + (m' - Y_v')\dot{v}' - (Y_r' - m'\,x_G)\dot{r}' = Y_\delta'\,\delta \tag{10a}$$

$$-N_v'\,v' + (N_v' - m'\,x_G')\dot{v}' - (N_r' - m'\,x_G')r'$$
$$-(I_z - N_r')\dot{r}' = N_\delta'\,\delta \tag{10b}$$

In the above Eq. (10) there are two new terms. The non-dimensional force from the $Y'_\delta\,\delta$ and $N'_\delta\,\delta$, the non-dimensional force and moment due to the rudder action. Representation of non-dimensional forces and moments are as per the standard book of Naval Architecture (Lewis, 1989). Eq. (10) are highly relied upon to manipulate heading and transverse position mainly using rudder and other control surfaces if applicable. All the notations and terms non-dimensionalised wherever necessary are as per (Lewis, 1989) Section 3 with title 'Motion stability and Linear equations', in Vol. III.

In non-linear theory Eq. (9) are modified as follows

$$X = X(\Delta u, v, r, \dot{u}, \dot{v}, \dot{r}, \delta) \tag{11a}$$

$$Y = Y(\Delta u, v, r, \dot{u}, \dot{v}, \dot{r}, \delta) \tag{11b}$$

$$N = N(\Delta u, v, r, \dot{u}, \dot{v}, \dot{r}, \delta) \tag{11c}$$

where $\Delta u = u - u_1$

## 3.1 Problems in Restricted and Laterally Confined Waters

Ship squat in open, depth restricted and confined waters has been discussed [14]. There will be loss or propeller rpm and speed. The sluggish behavior of ship in confined waters is to be considered while designing approach channels. If the bottom is rocky more clearances are to be provided. As already mentioned, additional expense will be incurred in dredging a rocky sea bottom for more depth. Squat is dependent on the block coefficient and speed of the moving vessel. A variable known as blockage factor also influences the squat value. Rough estimates of stopping time and stopping distance can also be calculated using empirical formulas.

It is a well known fact that wherever there is a finite water depth, the manoeuvring model is to be altered. The hydrodynamic derivatives for deep waters are to be corrected in the maneuvering equations already mentioned [15]. The following are the correction factors.

$$\frac{Y_{\dot{v}}'}{Y_{\dot{v}_\alpha}'} = K_0 + \frac{2}{3}K_1\frac{B}{T} + \frac{8}{15}K_2\left(\frac{B}{T}\right)^2 \tag{12}$$

Where B and T are the breadth and draft of the vessel.

$$\frac{N_{\dot{r}}'}{N_{\dot{r}_\alpha}'} = K_0 + \frac{2}{5}K_1\frac{B}{T} + \frac{24}{105}K_2\left(\frac{B}{T}\right)^2 \tag{13}$$

$$\frac{Y_v'}{Y_{v_\alpha}'} = K_0 + K_1\frac{B}{T} + K_2\left(\frac{B}{T}\right)^2 \tag{14}$$

$$\frac{Y_r'}{Y_{r_\alpha}} = K_0 + \frac{2}{3}K_1\frac{B}{T} + \frac{8}{15}K_2\left(\frac{B}{T}\right)^2 \tag{15}$$

$$\frac{N_v'}{N_{v\alpha}} = K_0 + \frac{2}{3}K_1\frac{B}{T} + \frac{8}{15}K_2\left(\frac{B}{T}\right)^2 \tag{16}$$

$$\frac{N_r'}{N_{r\alpha}} = K_0 + \frac{1}{2}K_1\frac{B}{T} + \frac{1}{3}K_2\left(\frac{B}{T}\right)^2 \tag{17}$$

where

$$K_0 = 1 + \frac{0.0775}{F^2} - \frac{0.0110}{F^3} \tag{18}$$

$$K_1 = -\frac{0.0643}{F} + \frac{0.0775}{F^2} - \frac{0.0110}{F^3} \tag{19}$$

$$K_2 = \frac{0.0342}{F} \tag{20}$$

and

$$F = \left(\frac{H}{T}\right) - 1 \tag{21}$$

where, H is the depth of water, T is the ship draft and B is the breadth of the ship.

In equations (12)-(21) the numerator is the non-dimensional hydrodynamic derivative for shallow water and denominator is that for deep water depth. It is found that all the values are not very useful for various restrictions of water around the hull. There is scope to improve the values of the shallow water hydrodynamic derivatives discussed already.

## 3.2 Control System Onboard

The rudder, other control surfaces and devices like bow thrusters are important features in achieving controllability goals. The rudder action is the most important component in achieving desired course either by changing or keeping the rudder at a deflected condition. Figure 4 shows the components of a control system.
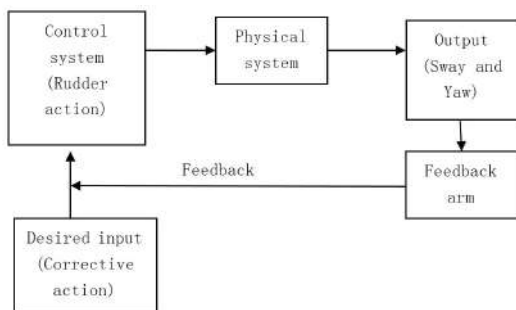


**Figure 4.** Components of control system

The rudder position in fact becomes the input and its turning rate can be improved by using high power hydraulic pump in the steering gear system. Basic difference be-

tween a massive rudder and a fin is that the inertia for the former is very large and that of the fins are usually small. Large power rating is required for ship rudders.

In electro-hydraulic systems used to control actuators, two factors are to be addressed separately. They are the sensitivity of the system and economy in operating the vessel. The former refers to modulation of the system. That is for a small deviation of heading from the steady state the opposing force and moment by at the turn of rudder should be of suitable magnitude. That means it should not be very high all of a sudden. If it is very high, the ship also will react unusually with a zero phase lag. In such a voyage the distance travelled will be more for a movement from port A to port B. It will tax unduly on the machinery causing more wear and tear with more consumption of lubricants and oils. Moreover, repeated and expeditious action by the crew is likely to lead to errors due to fatigue. Hence, a suitable controller like fuzzy logic can be recommended.

## 4. Application of Fuzzy Logic

After introduction[16] fuzzy logic has been widely used for many industrial applications. The Japanese used fuzzy logic extensively in many domestic and later in industrial products. A fuzzy- logic controller associates various sets of input data into a system with the desired control actions. Crisp or quantitative input data is converted into appropriate fuzzy or qualitative data. These are processed logically so as to produce a desired output. This output is to be brought back to a crisp form again. It is done by a de-fuzzification technique. Logical processes are simulated by rules, which associate different input data with a desired output. 'If – then' rules are applied for a sample case as follows.

a) If the heading is low and positive

b) If the shift in position is small and positive

-then the rudder angle is small and negative

The rate of position change and heading change can also be included in the conditions. All can be suitably clubbed to form decision tables. There are standard literature is available on this topic. The implementation of fuzzy logic was introduced decades ago in robots, machineries etc.

Low, medium, high etc. are converted into numerical values. Quantitative, numerical or crisp data is converted into qualitative, logical or fuzzy data. The standard practice to fuzzify input or output is to define membership functions. Membership functions associates the degree of belonging to any crisp value of some variable. Position error is shown in Figure 5 with membership functions. Membership functions are scaled from 0 to 1.0. Low value is 30 m from the reference line. Medium is 60 m and high

is 90 meters from the reference line respectively. For high with a membership value of 1.0 refers to 90 m or more than that. With a membership value of 0.5 high position error is 75 m as per the relevant figure.

Similarly the membership values are plotted for rate of position error, heading error and rate of heading error in Figure 6, Figure 7 and Figure 8 respectively.

The required rudder angle is determined using fuzzy logic for a set of position error, rate of position error, heading error and rate of heading error. This rudder angle is fed into the governing equations. The outputs obtained are heading, positions and associated velocities and accelerations.
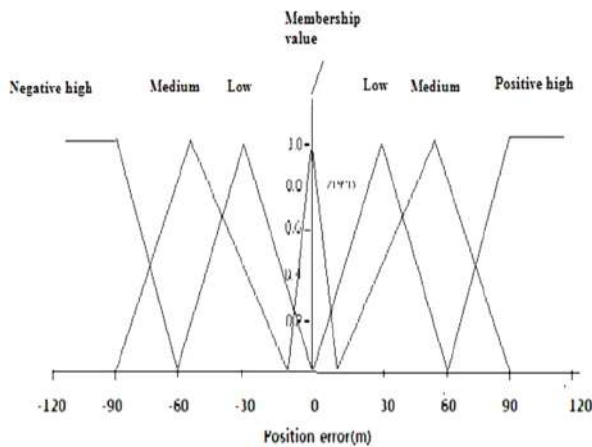


**Figure 5.** Membership function of position error
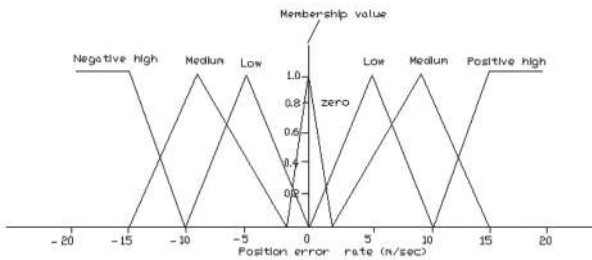


**Figure 6.** Membership function of position error rate
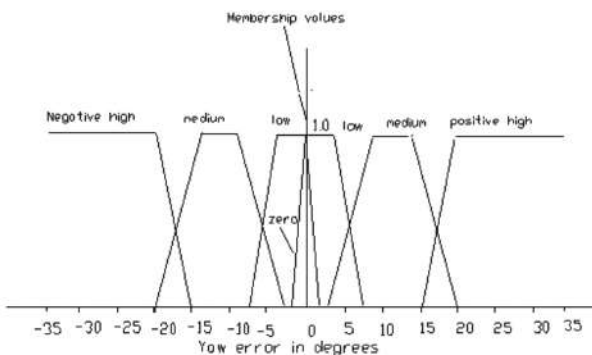


**Figure 7.** Membership value of heading angle error
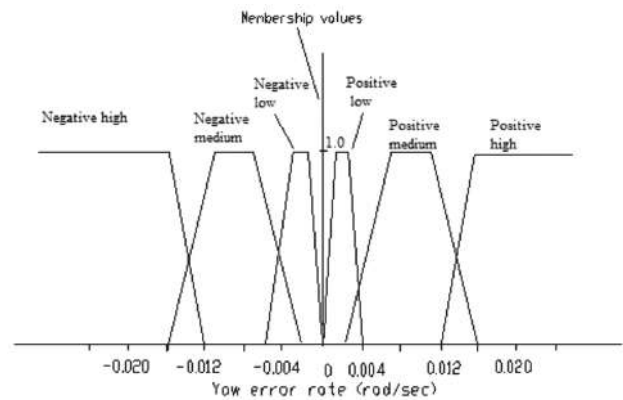


**Figure 8.** Membership function values of error rate of heading angle

## 4.1 De-fuzzification

For de-fuzzification, there are six most often used approaches [17] as follows.

1) The centre-of-area method which is also called the centre of gravity method.

2) Centre-of-sums de-fuzzification

3) Centre of largest area de-fuzzification

4) First of maxima de-fuzzification

5) Middle of Maxima de-fuzzification

6) Height de-fuzzification

Among these the first one is the best well-known de-fuzzification method and more accurate since it covers all the events in the fuzzy sets of membership functions. Here the angle of deflection of the rudder angle is to be determined from a membership sets plotted against the domain. The domain range is maximum and minimum rudder angle. Similarly heading angles can also be chosen from another sets of membership functions. The linguistic variables are converted into crisp values. It is to be noted that the inputs and outputs are passed through a transfer function like box, which governed all the manoeuvring theory. The membership functions of rudder angle and vessel heading are similar to the membership functions are

A linguistic variable is defined by

$(U, £U, u, M_u)$                                    (22)

Here U denote the symbolic name of a linguistic variable. £U is the set of linguistic values that U can take on. A linguistic value denotes a symbol for a particular property of U. Arbitrary element of £U is denoted by LU. $u$ is the actual physical domain over which the linguistic values are meaningful. Mu is a semantic function which leads to an interpretation of a linguistic value in terms of quantitative elements of $u$.

It is possible to write $M_u : LU \rightarrow \overline{LU}$, where $\overline{LU}$ is a

denotation for a fuzzy set or membership function defined over $u$.

That is $\overline{LU} = \sum \mu LU(u)/u$ in the case of discrete $u$.   (23)

And $\overline{LU} = \int_u \mu LU(u)/u$ in the case of continuous $u$.   (24)

$M_u$ is a function which takes a symbol as its argument and returns the strength of this symbol in terms of a fuzzy set. The centre of gravity is method is applied here as it is powerful and gives reasonable results for a problem like this.

Now the fuzzy set of a number of rules can be defined in the 'if-then' form. Here it is possible to concentrate on the heading angle and rudder angles. 49 sets of rules for are formulated in each case. Two tables of 7*7sets of membership values and plots against the respective domains are prepared. The table dimensions depend on the number of rules used. The advantage of fuzzy rule is that there is flexibility in using the number of rules and there is an optimum level for the same. The shape of membership functions are as shown for position and heading. For linear case it is of the shape of triangle and trapezium. For the inputs considered in this problem both were used and there was no appreciable result found for change in the shape membership function from all triangle to all trapeziums or vice-versa or even combination of both. Easiness in mathematical representation in the code is another factor to choose the shapes of membership function. The de-fuzzification part was incorporated in the C++ code and the output us directed into a Matlab code for plotting. The code in C++ is run for stretch of 6km length to cover the entire approach channel. The code can be used for any reasonable lengths of channel. Therefore, after making and running the code, still modifications are easily possible for the channel parameters. Fully loaded cases are discussed. In the ballast condition wind load may be higher, but it is of lesser important in other aspects.

### 4.1.1 Control Algorithm Based on PID in Brief

PID control defines the relationship between the input and the output variable as follows.

$\quad$ i = $K_p(e)$+$K_d(\dot{e})$+$K_i \int e(t)dt$          (25)

where, i is the input variable, Kp is the proportional constant P, Kd the derivative constant D, Ki the integral constant I, e the instantaneous error and the instantaneous time derivative of error. Here, the input is the rudder angle and the output is the yaw angle and position co-ordinates and the physical system is represented by the governing equations. Figure 4 illustrates the positions of the control boxes of the system. A code is developed separately for PID control system in C++ and the problems worked out using fuzzy logic is done using the PID control algorithm.

In all cases, the results are comparable and in the next part only typical results are compared and presented to optimize the space in this paper.

The control constants Kp, Kd and Ki have various effects on the system. Kp reduces the time taken to reach the desired output but results in overshoot. If Kp alone is used neglecting the other control constants, it cannot provide convergence due to the existence of a steady error. The integral constant, Ki, may be used to eliminate a steady error but it will result in an adverse transient response. Kd improves stability of the system, reduces overshoot and improves the transient response. In some cases all these control constants are needed for a successful design. There is scope for tuning of these constants so as to achieve a reasonable and comparable result of parameters of ship navigation. The control constants can also be represented as physical parameters like mass, natural frequency in particular mode, time period etc. of the ship[11]. Such approach will provide guidelines to choose proper initial values for trial and error exercise of tuning.

### 4.2 Results and Discussion

As already discussed, a global system of fixed co-ordinates system is usually assumed for simulations. A few cases of arrival and departure in the approach channel is considered. Initial conditions of the vessel, that is heading and shift of its CG from the centerline of the channel, and intended speed are given as input to the code before running. A few cases are worked out and displayed.

A 6km distance is considered for the simulation which take 1500 secs. Less than half the full speed of ship is considered. It is 8 knots and which is considered to be suitable for the approach channel, however, it may vary port to port. A co-ordinate system is assumed to be the x direction at the centre line of the ship. Perpendicular to this is taken as the lateral direction. The ship body force is countered by the external loads.

In Figure 9, the vessel is at the centre line of the path and is turned by 10 deg. to one side. It can be assumed as a result of the environmental disturbance. However, for various ships this turn in heading may vary due to their superstructure heights, forecastle shape etc

Next case of a fully loaded arrival is shown in Figure 10. The ship's initial heading is 5deg and CG is shifted by 20m from the centre line. The disturbance is bit stronger because of initial sway by 20m. The ship is under control within 1500 secs.

Another case is shown Figure 11 for an initial heading of -5 deg and shift of -15m, which is somewhat opposite to the previous case. The ship is seen to be under control in reasonable limits of time and space.
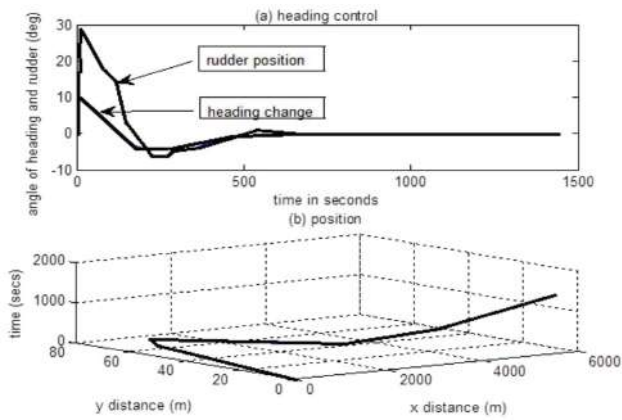
**Figure 9.** Fully loaded arrival, no shift from CL of path, but tilted 10 in heading
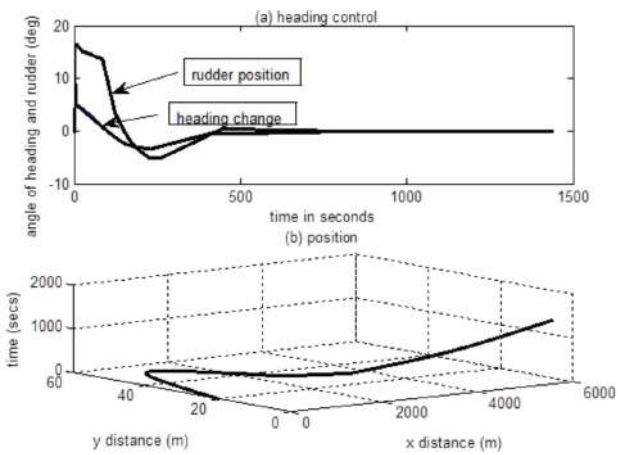


**Figure 10.** Fully loaded arrival with 20m shift of CG from the CL of path, heading 5 deg
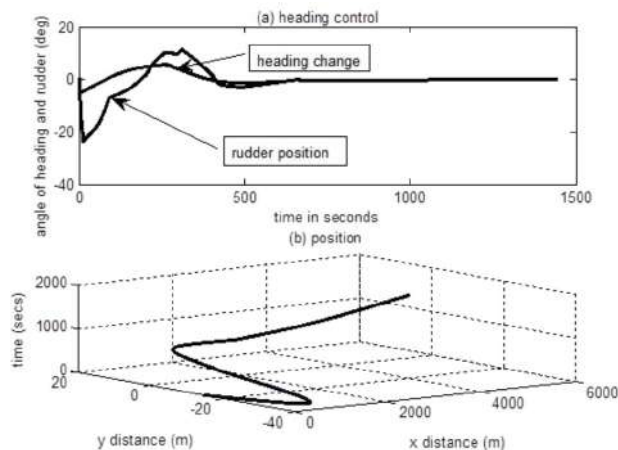


**Figure 11.** Heading -5deg and shift from CL -15m, fully loaded arrival

A number of cases have been simulated using the code which mimics the presence of a captain onboard ship.

Ballast conditions are also simulated using the code de-

veloped. Heading angle is turned by -5 deg and the position is shifted by -20m. The vessel is brought into the desired path by activating the rudder within a desirable time and is shown in Figure 12. Another initial condition of heading change by 10 degree and the cg of the vessel is in the midline of the approach channel. In all these simulations, an analyst or designer should look at the clearances from the sides of 200m lane. The vessel clearance by from the outer limit of channel is determined from the ships frame superposed on its trajectory with the ship's centre line as a tangent at the point of interest. Thus, the tangent with the relevant heading angle will give the ship' actual positions with its frame superposed. The centre of gravity can be assumed point at which the tangent is made. The CG is plotted to avoid congestion of closely packed lines of the outer hull of hip. The timing is also a factor since controlling the vessel in shallow water is difficult. But the output of the code gives reasonable results. Sufficient lateral clearances from the outer border of approach channels are ensured in all cases. Any number of simulations can be repeated similarly.
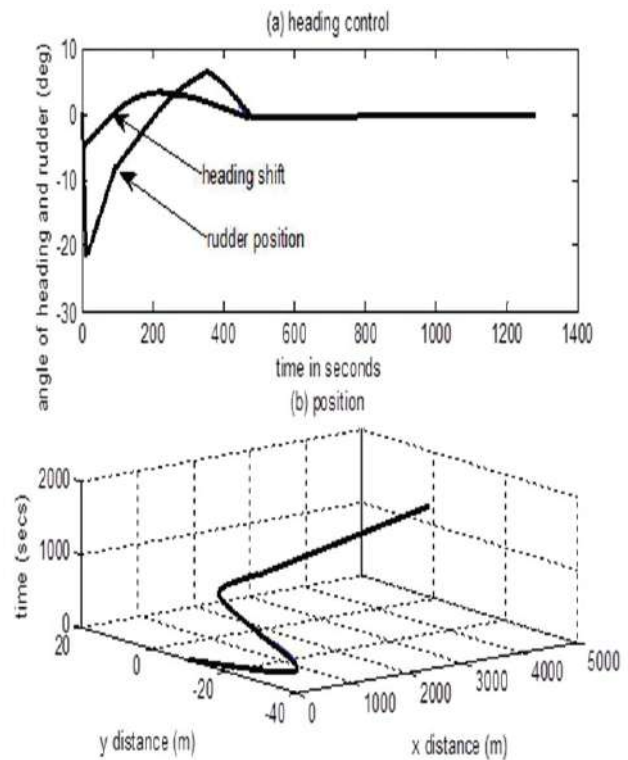


**Figure 12.** Ballast departure heading -5 deg and shift -20 m

The code is capable of giving velocities and accelerations. Such details are helpful to verify or to arrive at the hydrodynamic derivatives, which govern the trajectory of the ship. For a fully loaded arrival condition, the trajectory and heading angles have already been shown

in Figure 9. The same problem is worked out using PID algorithm of control. In PID maximum rudder angle is 25 degrees while that in fuzzy logic control it is nearly 30 degrees. PID is a well established procedure for control engineering of plants and in fuzzy logic the trajectory in y-direction is much more. It shows that there is scope for improving the method.
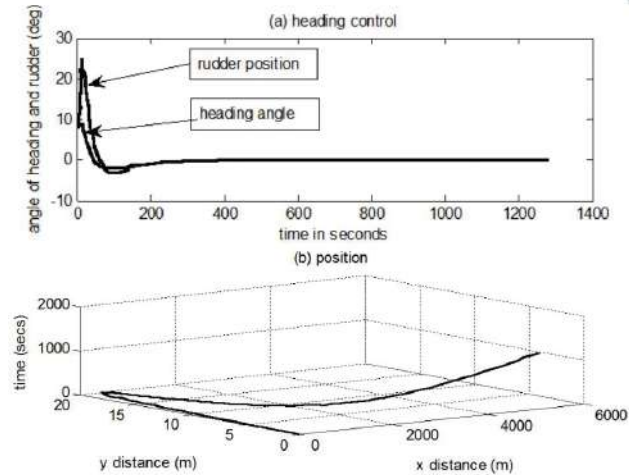


**Figure 13.** Trajectory and heading under PID for comparison.
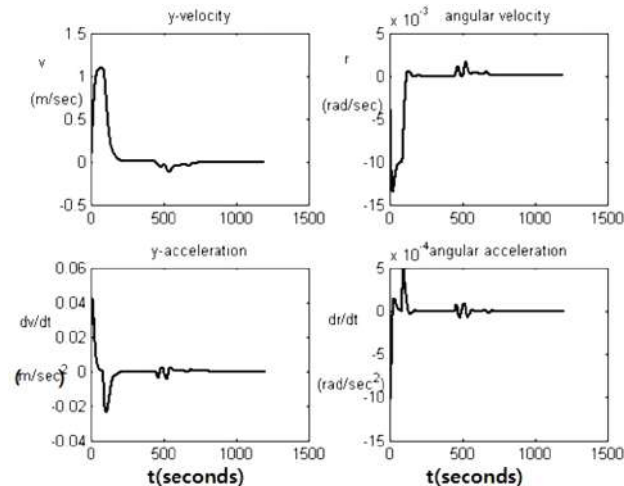


**Figure 14.** Ship velocities and accelerations using Fuzzy logic

Figure 14 is shown the kinematic details of the system for fully loaded arrival at 8 knots and the ship is controlled by fuzzy logic algorithm. The ship velocities and accelerations as PID system are shown in Figure 15. The velocities and accelerations are plotted after the rudder action as a result of ship's disturbance due to an external force. In fuzzy logic the lateral velocities are of more than 1.0m/sec and that of PID is 0.075m/sec. Though drastic variation is seen in transient condition but later both converge into negligible values. The initial condition of any dynamic system is unpredictable till it reaches a steady

state condition. It can be seen that the angular velocities and accuracies are also comparable for both approaches. The comparison shows that fuzzy logic can still be improved by admitting more membership functions and decision matrix in the code.
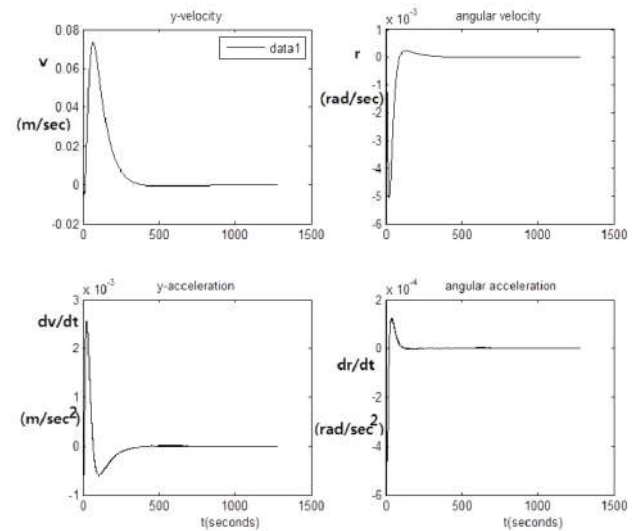


**Figure 15.** Ship velocities and accelerations using PID control

## 5. Conclusions

Initiation of setting up of a new port and harbor facility along the east coast of India is discussed for a design ship. Waterway is decided for a design ship and is based on the requirement of international bodies. A powerful algorithm based on fuzzy logic is discussed. Standard linear maneuvering equations are used in C++ code. The control system works on fuzzy logic. Shallow water and confined water effects are discussed. The most powerful de-fuzzification method is discussed and implemented.

First 22 km length of the approach channel, 4 to 6 km stretch till the entrance of harbour is analyzed using manoeuvring model. The trajectories of a fully loaded bulk carrier at 15m draft are demonstrated. The vessel trajectory in ballast condition also is demonstrated. The clearances, speed, accelerations are found to be reasonable. Such kinematic details are very much useful for analysts to arrive at added masses and other hydrodynamic derivatives. These are all very important for the designers to provide the strength of fenders, dolphins etc.

The manoeuvring clearances for single lane passage are found to be of reasonable values. The model has provisions to add on additional environmental effects. It is possible to find the trajectory in rough weather acting perpendicular to the ship while the ship is entering the main harbour mouth. There is provision for superposing the environmental forces.

A vital part of technology in the immediate future in

the automation of ship manoeuvring and control is demonstrated here with case studies.

The model is compared with the well established PID control system and is found that the trajectories, velocities and accelerations are comparable. There is room for improving the accuracy of model using fuzzy logic principle.

Fuzzy logic based model is a general one and versatile in the sense that it can be used for any other channel-ship combination with suitable changes in the hydrodynamic parameters of the ship considered.

**Author contributions.**

The work was done by single author and the topic was a continuos passion for the author.. Other unpublished part of the work is retained in view of optimization of space.

**Conflict of interest.**

There is no conflict of interest for this work.

**References**

[ 1 ] Abkowitz, M.A. Lectures on Ship hydrodynamic-Steering and maneuverability, Hydro-Og aerodynamisk Laboratorium, Report Hy-5, Lyngby, Denmark, 1964.

[ 2 ] Eda, H and Crane , Jr. C. L. Steering Characteristics of Ships in calm water and in Waves. SNAME Transactions, 1965, 73.

[ 3 ] Clarke, D., Gelding, P., and Hine, G. The application of maneuvering criteria in hull design using linear theory. Trans. Royal Institutions of Naval Architects Trans, 1982.

[ 4 ] Biancardi, C. G. Practical calculation method of ship maneuvering characteristics at design stage, Faculty of Nautical Sciences, Instituto Universitario Navale, Naples, Italy, 1989.

[ 5 ] Fossen, T I. Guidance  and control of ocean vehicles. John Wiley & Sons, 1994.

[ 6 ] Khac Duc Do and Jie Pan. Control of ships and underwater vehicles.-Design for underactuated and non-linear marine systems.Springer-Verlag London Ltd, 2009.

[ 7 ] Alexander I. Korotkin. Added Masses of Ship Structures. Springer Science & Business Media. B. V, 2009.

[ 8 ] Daniel A. Liut, Owe F. Hughes, Dean T. Mook. Control of Rolling in Ships by Means of active fins governed by a fuzzy-logic controller. Journal of Ship Research, 2001, 45(4), 279-288.

[ 9 ] Gyoungwoo Lee, S. Surendran and Sang-Hyun Kim. Algorithms to control moving ship during harbor entry. Applied Mathematical Modelling, 2009, 33, 2474-2490.

[10] Fossen T I. Handbook of marine craft hydrodynamics and motion control. John Wiley & Sons. Ltd, 2011.

[11] Bruce L. Mc Cartney et al. Ship Channel Design and Operation, ASCE, USA, 2005.

[12] Anthony F. Molland. Maritime Engineering reference book. A guide to Ship Design, Construction and Operation, Elsevier, 2008.

[13] Gregory P. Tsinker. Port Engineering, Planning, Construction, Maintenance and Security. John Wiley & Sons, 2004.

[14] Barass C, B. Ship Design and Performance for Masters and Mates. Elsevier Publishers, 2002.

[15] Clarke, D., Gelding, P., and Hine, G. The application of maneuvering criteria in hull design using linear theory. Trans. Royal Institutions of Naval Architects Trans,1982.

[16] Zadeh L. A. Fuzzy sets. Information and control.8 338-353. University of California, Berkeley,1965.

[17] Driankov D, Hellendoorn and Reinfrank M. Introduction to fuzzy logic. Narosa publishing House, New Delhi,2001.

## ARTICLE

# Corrosion Control of Coated Structural Components in Marine Environment

**G. L. Manjunath[1]   S. Surendran[2]***

1. Department of Ocean Engineering, Indian Institute of Technology Madras, Chennai, India
2. Department of Ocean Engineering, Indian Institute of Technology Madras, Chennai, India

ABSTRACT

Tropical waters are with more salinity and harbor millions of micro organisms. Such environmental condition challenges the strength and reliability of marine structures. The behaviour of structural materials due to pitting and uniform corrosion is studied, and a method based on coating is suggested to improve the life cycle ensuring reliability in its functionality. The structural materials like high strength steel and AA6063 were selected for the study and metallic coating performed for evaluation of corrosion resistances. Samples are investigated in chloride concentration of 3.5% NaCl by weight loss measurements and potentiodynamic polarization. The coating was done by electroplating and PVD (Physical Vapour Deposition) method for high strength steel, where as aluminum samples were coated by an electroplating method. The high strength steel samples were mono coated by Ni and Cr using the electroplating method, and composite coating was done with Al-N (Aluminium nitride) and Ti-Al-N (Titanium Aluminium Nitride) by PVD techniques. Scanning electron microscopy (SEM) was used for evaluation of fracture toughness of coating around the pits formed. The investigation showed that the methods and thickness of coating influenced corrosion resistances of the substrate metals. Composite coated samples by PVD showed excellent corrosion resistance properties compared to electroplated samples after the investigations. Finite element analysis was performed by FRANC 2D/L (Fracture Analysis Code) showed a decrease in stress intensity values for composite coated samples of PVD compared to mono coated electroplated samples. Increase in the duty cycle of the structure was observed in the simulation has a result of a decrease in stress intensity values for PVD coated samples.

## 1. Introduction

The reliability and serviceability of marine structures are always challenged in the marine environment due to corrosion. Corrosion degrades the performance of the structural components for different loading conditions. The corrosion induces fatigue due to variable loadings is another challenge to the designer as this leads to premature aging of structures. And aging may lead to the growth of single and multiple cracks with different types of loading. As the metal corrodes the crack tip may get blunt which may lead to sudden failure or branching of cracks and the repair of these types of

*Corresponding Author:*

*S. Surendran*

*Department of Ocean Engineering, Indian Institute of Technology Madras, Chennai, India*

*Email: sur@iitm.ac.in*

failures becomes difficult. The effective performance of structural components in the severe marine environment is a matter of concern and corrosion as become a major area of study. Petroyiannis et al.[1] focused on the mechanical behavior of corroded aircraft components AA2024 by conducting experiments. A moderate reduction in yield, ultimate tensile stress, and strain energy density are observed due to a reduction in thickness. Reduction in mechanical properties does not affect the tensile ductility, and experiments suggest that corrosion is due to hydrogen embrittlement. Some researchers developed a mathematical model for explaining the multi-scaling concepts like fracture toughness, residual strength, and strain energy density. Pantelakis et al.[2] evaluated the corrosion susceptibility of aluminum alloys used in aircraft structures and calculated tensile and energy density data. Samples were pre-corroded by accelerating corrosion tests and found a decrease in yield and ultimate tensile stress. Authors found that hydrogen penetration and absorption was the main reason for material degradation and volumetric embrittlement. Birchon [3] briefly reviewed on the selecting nature of materials and fabrication processes on the performance of structures in ocean engineering. The author also emphasized the material weakness and capabilities in offshore, due to corrosion induced fracture and fatigue.

Harlow and Wei [4] discussed the effects of pitting corrosion and its effects on the durability and integrity of structures. Authors studied the rate of pit growth and proposed some probability models for the growth of corrosion pits in aluminum alloys in aqueous environments. Statistically estimated the size of the corrosion pits at a given time for multi-site damage and cracked growth by proposing a mathematical model. Pidaparti and Rao[5] investigated the corrosion damage in structural components like aluminum and steels used for aerospace and naval structural applications. Authors used CAD (Computer Aided Design) for modeling the pits and FEM (Finite Element Method) for predicting the stresses in single and multiple pits. The analysis was done for estimating stress distributions on the corroded surface as a function of time and sample surface layers. Authors observed the formation of micro cracks around the main pitted area this lead to nucleation and coalescence of fine cracks and finally resulted in differential stresses along the sample thickness. Gooch and Booth [6] paid attention to the aspects of offshore design and corrosion fatigue of steel structures. Authors studied the variable effects like cyclic stress conditions, environmental factors, and material characteristics and their influence on structural response. Lynch [7] studied some cases of failures and generalized the procedures to analyze failures. They suggested a procedure to over-come the shortcomings due to stress cracking. Corrosion fatigue, hydrogen embrittlement and liquid-metal embrittlement in aluminium alloys, high-strength steels etc, . were the topic of interest to the author. Moan, and Uraga [8] addressed ship hull maintenance under combined crack growth, corrosion on structural components by proposing a reliability-based model. Reliability model takes into account of corrosion-induced crack growth rate in two ways increase in stress range by the plate thinning and corrosion induced fatigue. Sensitivity studies and hazard rate concept were adopted with different case studies by inspecting the hulls at regular interval of time. Dale et al. [9] demonstrated the corrosion damage assessment framework for aging aircraft structures they evaluated several tools like FRANC2D/L for stress distribution, AFGROW for fatigue crack growth and PROF for the probability of fracture. The structural analysis was done for crevice corrosion and multiple site damage in fuselage lap joints and compared with experimental results and showed a good agreement in the interesting parameters.

Gangloff [11] discussed modern laboratory testing techniques for corrosion fatigue and their principles and mechanisms involved. Emphasis was given to specimen design, loading, environmental controls, strain and crack size measurements later on data analysis and interpretation. The author showed the complexities associated with the corrosion fatigue effects in the performance of structural metals. Zaid et al. [16] studied the corrosion behavior of AA6061 alloy considering the effect of pH and chloride concentration of NaCl solution by weight loss measurement tests, potentiodynamic polarisation, linear polarization, and cyclic polarisation followed by SEM analysis. Authors found that pH and chloride concentration of NaCl solution affected the corrosion behavior of AA6061 alloy. Hemispherical and cryptographic pits were formed as a result of localized corrosion. Tamura et al. [17] concentrated on models for explaining corrosion reactions. This included the formation of rust and pH effect on the corrosion rate. Authors paid attention to the rust films stoppage and passage of anions by deteriorated rust film separation of cathode and anode leading to crevice corrosion. Pidaparti et al.[18] suggested nondestructive testing techniques for structural health maintenance of structure using image analysis for studying the corrosion morphology by wavelet transformation and fractals useful for correlating service and failure conditions. Authors studied on pits formation and initiation and growing cyclically leading to material failures based on corrosion conditions and applied stress. Allachi et al.[19] studied the uniform and pitting corrosion processes on AA6060 alloy in the presence of small concentrations of cerium chloride to

3.5% NaCl. Authors mainly focussed on the determination of the protection and inhibition character of cerium ion by SEM and EDS spectra. Park[20] studied the structural integrity of aging ships by focussing the study on corrosion, fatigue cracking and formation of local dents developed during the time of ship service. The risk assessments of the ships were aimed by studying the ultimate strength characteristics of the ship structure. Paik and Kim[21] developed a corrosion wastage model by understanding the phenomenon of aging of the ballast tank structures. The proposed model was able to predict the time-dependent corrosion wastage accurately. The study was helpful in judging the performance of the ship in the marine environment and periodical inspection with the ship structures for safe operations. Mohd Hairil Mohd et al.[22] used magnetic flux leakage tool for as a nondestructive evaluation (NDE) technique for evaluating the corrosion depth and width in gas pipelines. The NDE techniques help in accurate predictions of the reliability of the aged structures. Authors developed some time-dependent corrosion models for estimating pitting corrosion depths by undergoing statistical studies. The proposed model predicted the pit depth at any given age just by changing scale, shape and location parameters. The above inputs help in designing a new gas pipeline saves a huge amount of risks, economy and time. Manjunath and Surendran [23] metallically coated samples were exposed to different temperatures and corrosive environment, and a difference in dynamic fracture toughness values was noted. The method of coating influenced the performance of the substrate metals.

Currently, in the present work, high strength steel and AA6063 samples were coated with two different methods of coating like electroplating and PVD (physical vapor deposition). The high strength steel samples were electroplated by Ni (nickel) and Cr (chromium) in steps of 6μ, 20μ, 40μ, and 60μ whereas PVD samples coated with a 6μ thickness only because of limitations. Aluminum samples were coated with Ni in steps of 6μ, 20μ, 40μ and 60μ. Samples were tested by potentiodynamic polarization. The samples which were coated with PVD showed excellent corrosion resistance in the case of potentiodynamic polarization and uniform corrosion. Later thinning effects were considered in the finite element analysis done using FRANC 2D/L. The fatigue crack growth life cycle of coated and uncoated samples was estimated before and after corrosion and compared.

## 2. Experimental & Simulation Details

Two types of testing were carried out in the present work, potentiodynamic tests for pitting corrosion and weight loss test for uniform corrosion. The required sample dimension for the potentiodynamic test is the 25.4mm diameter and 10mm thickness, and for uniform corrosion, it is 55mm length, 10mm width, and 10mm thickness. A V notch at the center of 2mm depth was considered. Samples are coated by PVD and electroplating for steel samples and in aluminum only electroplating is done. Steel samples were coated with Ni and Cr in electroplating and PVD composite coating of Al-N, and nano crystalline material of Ti-Al-N was done, for AA6063 alloys electroplating of Ni was done. The coating thickness was in the steps of 6μ, 20μ, 40μ and 60μ in electroplating. Only 6μ coating thickness was done using the PVD method.

Potentiodynamic polarization was done for all the samples of steel and aluminium and a corresponding graph of E (voltage) v/s I (current density) was obtained for each sample. Corresponding $E_{corr}$ and $I_{corr}$ values are obtained for each sample by drawing the tangents for anode and cathode curves, pitting corrosion rate for each sample was obtained. The steel samples were tested in 3.5% NaCl solution, and in case of aluminum samples were tested in 3.5% NaCl, and NaOH added to maintain the pH value while conducting the experiment (buffering the solution). For uniform corrosion, a weight loss test was performed for 2400 hours the weight of the samples were noted for calculating corrosion rate. The uncoated and coated samples of steel and aluminum samples were soaked in 3.5% NaCl with a pH value of 7.



**Figure 1.** (a) Electro chemical set up



**Figure 1.** (b) Sample along with cell components

**Figure 1.** (c) Samples corroded in 3.5% NaCl



**Figure 1.** (d) Samples after corroding for 2400 hours



**Figure 1.** (e) 6μ Coated samples of PVD and electroplated samples corroded for 2400 hours



**Figure 1.** (f) 20μ Samples of Ni and Cr corroded for 2400 hours.



**Figure 1.** (g) from left to right: uncoated sample of aluminum, 6μ Ni coated aluminum, 20μ Ni coated aluminum, 40μ Ni coated aluminum and 60μ Ni coated aluminum after corroding for 2400 hours

The figures 1 (a) and 1 (b) shows the cell set up along with arrangements for potentiodynamic polarization. In figures 1 (c) and 1 (d) the samples are corroded in 3.5% NaCl for 2400 hours and washed with distilled water thoroughly before seeing the weight of the corroded samples. Figure 1(e) showed how the sample is being corroded near notch and compared to other electroplated samples (on the right side) the PVD coated samples (to the left showed) more corrosion resistance. The 20μ electroplated samples of Cr sample to the right were better corrosion resistance compared to Ni samples to the left. Aluminum samples showed the phenomenon of deposition of salt on the surface. The salt is getting deposited on the surface of 6μ Ni coated aluminum samples. The removal of deposited salt from the surface can result in removal of the substrate. Comparatively, the coated samples are corroding fast compared to uncoated samples.

ASTM G-59 proposed standard test method for conducting potentiodynamic polarization resistance measurements [13]

$$\text{Corrosion Rate} = \left[ \frac{3.27 \times 10^{-3} \times i_{corr} \times EW}{\text{Density}} \right] \qquad (1)$$

Where corrosion rate is measured in mmpy, icorr is corrosion current density; EW is the equivalent weight of corroding samples, an area in mm$^2$ and density in g/cm$^3$.

Equation for uniform corrosion rate as per [14]

$$\text{Corrosion Rate} = \left[ \frac{1000 \times \text{Weightloss} \times 365}{\text{Time} \times \text{Area} \times \text{Density}} \right] \qquad (2)$$

Where corrosion rate is measured in mmpy, weight loss in grams, time in days, an area in mm$^2$ and density in g/cm$^3$.

Effective stress intensity factor Keffective is calculated for different crack lengths taken from [12]

$$K_{effective} = \sqrt{K_I{}^2 + \beta K_{II}{}^2} \qquad (3)$$

Where $K_I$ and $K_{II}$ are used to denote fractures in mode I and mode II and β co-efficient is the material characteristic [15]

$$K_{Ic} = 0.0319 \frac{P}{a\sqrt{c}} \qquad (4)$$

Equation (4) is used for evaluating the fracture toughness of coating much thicker than 1μ, the fracture toughness $K_{Ic}$ depends on applied load P and indenter size at which causing a crack c in the coating. The indentation is done by Vickers micro hardness tester on the coating before and after corroding. In pitting corrosion around the pits, the indentation was done to evaluate coating toughness around the pits later it was done for uniformly corroded sample near the notch area which was found to be weak. The pitting and thinning effects from the experiment are considered, and simulation is carried out in FRANC 2D/L. Uniform and pitting corrosion are considered individually for the different duration in some years, later the uniform and pitting are included together, and analysis was carried out. The analysis was performed for multiple cracks, and those with high $K_{effective}$ was considered for the study. Corresponding $K_{effective}$ (effective stress intensity factor) values in mode I and II is calculated differently for crack length. Fatigue crack growth simulation after the corrosion was done for multiple cracks and the crack which is showing the least number of cycles is taken.

## 3. Results and Discussion

The uniform and pitting corrosion tests were conducted to study the corrosion effect on crack growth due to cyclic loading responsible for the catastrophic failure of the structure. In pitting growth, a pit can cause the growth of other micro pits around it leading to multiple cracks. The phenomenon of multiple cracking is assumed in uniformly and pitting corroded samples individually due to corrosion. Both uniform and pitting corrosion is considered together for samples by assuming uniform corrosion to occur first followed by pit formation. To overcome the above problems a technique of coating is adopted in the present work; coating helps to reduce the corrosion rate thus enhancing the life of the structure. Selection of coating material depends on adhesive strength and depends on the ability towards corrosion. The permeability in coating decides the durability and transition temperature of the coating. Potentiodynamic tests on electroplated Ni aluminum samples showed the increase in corrosion resistance with an increase in coating thickness as per figure 2. The coated and uncoated samples of aluminum were tested

in 3.5% NaCl, and NaOH added to maintain the pH. The formation of pits can be seen in almost every coated and uncoated samples of aluminum.
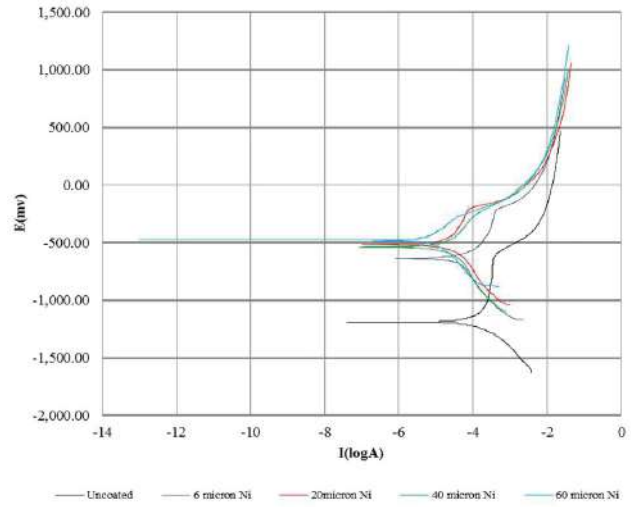


**Figure 2.** $E_{corr}$ Vs. $I_{corr}$ for coated and uncoated aluminum samples

The potentiodynamic polarization of electroplated steel samples showed an increase in corrosion resistance with an increase in coating thickness. Electroplated Ni samples of steel showed the formation of pits in all the coated samples with coating thickness varying from 6μ, 20μ, 40μ and 60μ shown in figure 3. In Cr electroplated samples of steel, pits are observed in 6μ, 20μ and 40μ samples except in 60μ case. When the PVD coated samples were tested, the 6μ Al-N steel coated sample showed a slight wearing out of the surface due to corrosion, and in 6μ Ti-Al-N no such phenomena were seen thus was a case of excellent corrosion resistance.
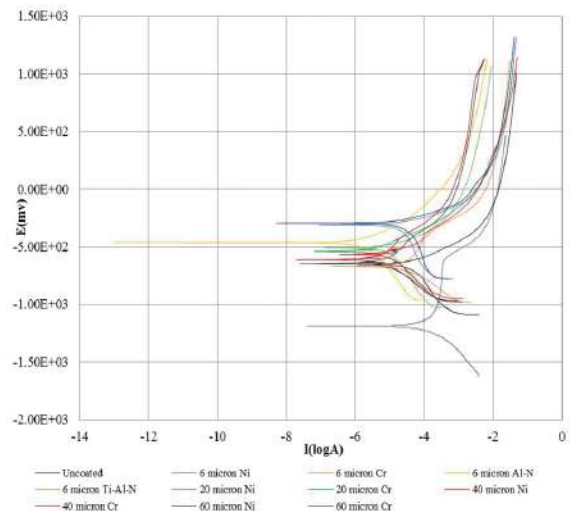


**Figure 3.** $E_{corr}$ Vs. $I_{corr}$ for coated and uncoated steel samples

After the weight loss experiment, the corrosion rate against corrosion time was plotted for uniform corrosion of both coated and uncoated samples. Parent metals of steel and aluminum were considered, and equation two was relied upon. In the case of Ni and Cr electroplated steel samples the increase in coating thickness reduced the corrosion rate and in PVD coated Al-N and nano crystalline Ti-Al-N steel samples was found to be still shown in figure 4. In Ni electroplated sample of aluminum the salt started to deposit on the 6μ Ni coated samples. No salt deposition was observed in uncoated samples of aluminum. Removing the deposition of salt from samples in 6μ Ni coated samples resulted in the removal of substrate material. For aluminum this is equivalent to an increase of corrosion rate.
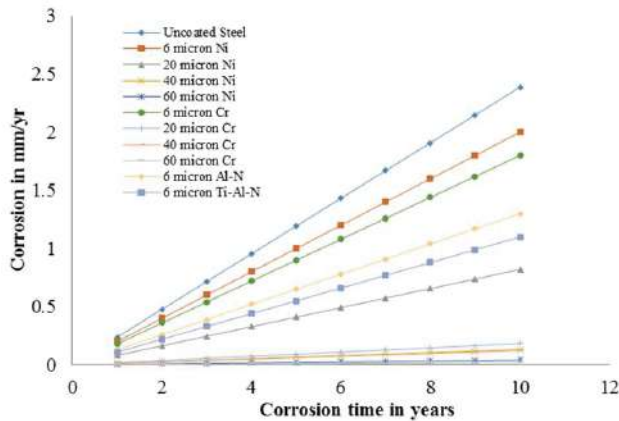


**Figure 4.** corrosion rates against corrosion time for uniformly corroded steel samples
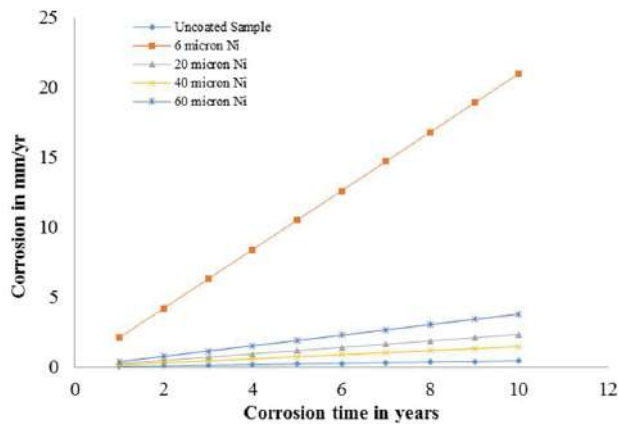


**Figure 5.** Corrosion rates against corrosion time for uniformly corroded aluminum samples

As per the potentiodynamic polarization, the pitting corrosion rate against time is reduced due to an increase in coating thickness. For coated and uncoated steel and aluminum samples a comparison of figure 6 and seven will easily convince this.
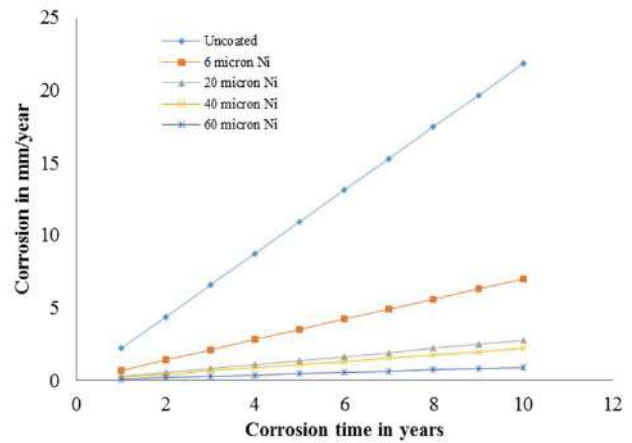


**Figure 6.** Corrosion rates against corrosion time for pitting corroded aluminum samples
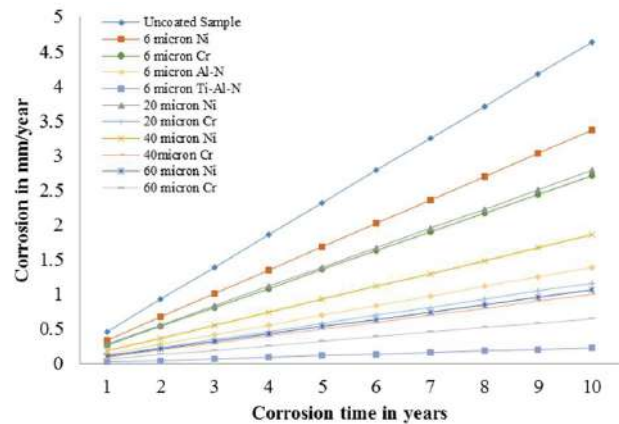


**Figure 7.** Corrosion rates against corrosion time for pitting corroded steel samples

Different combinations of corrosion rates, pitting and uniform corrosion are considered by deducting the thickness from the sample. The increase in thickness shows an increase in corrosion rate and reduced performance of the structural components. The corrosion rate against corrosion time is plotted considering the combination is shown in figure 8 and figure 9 for steel and aluminum. The steel samples showed an increase in corrosion rate compared to aluminum shown in figure 8 and 9. The influence of coating thickness on corrosion is proved here, through not directly. Classification societies insist on the renewal of plates, stiffness and structural part based on the diminishing of thickness on a percentage basis. It varies from location to location on ship hull contour.

Tropical waters deteriorate the hull structure more rapidly compared to the Arctic, North Atlantic waters, etc. Hull designers will more be interested in the mechanical strength properties of steel and aluminum after getting corroded. Next part deals with the variation in fracture
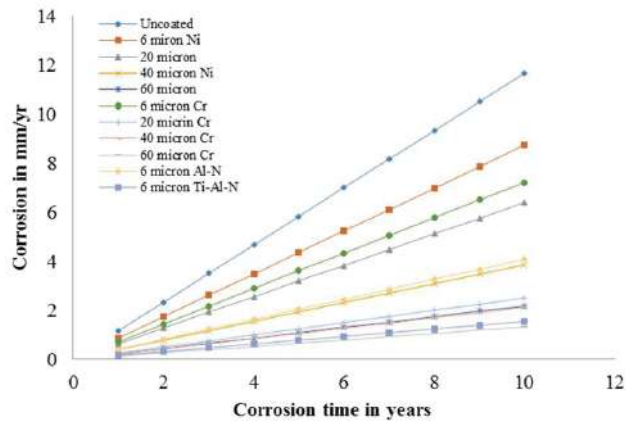
**Figure 8.** Corrosion rates against corrosion time for pitting and uniformly corroded steel samples
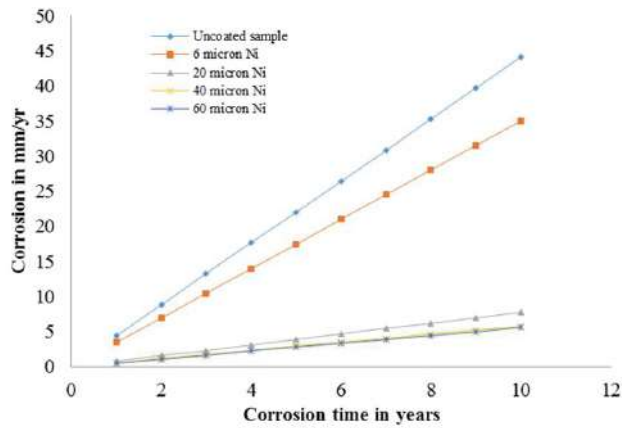


**Figure 9.** Corrosion rates against corrosion time for pitting and uniformly corroded aluminum samples

toughness due to the diminishing of thickness due to corrosion. The simulation was done by FRANC 2D/L, and the corresponding $K_{effective}$ against crack lengths were calculated for uniform and pitting corrosion initially, and later both were combined. $K_{effective}$ against crack lengths is calculated for 1 and five years respectively for coated and uncoated samples of steel and aluminum. $K_{effective}$ values found increasing with increase in corrosion time for uncoated samples. Coated steel samples showed a decrease in $K_{effective}$ with an increase in coating thickness in case of an electroplated sample of steel from figures 11 and 12. In figures 11 the value of $K_{effective}$ is found less compared to figures 12 in which the $K_{effective}$ is found increasing due to increasing in corrosion rate. The Al-N and Ti-Al-N samples showed corrosion resistance with coating not getting peeled off near the notch, while in electroplated samples peeling of coating near the notch can be observed in case of steel samples. Multiple cracks were grown near the uniformly corroded area and crack with high $K_{effective}$ was

considered for the analysis. The reduction in thickness of sample will affect the $K_{effective}$ values and even cause a grouping of cracks.
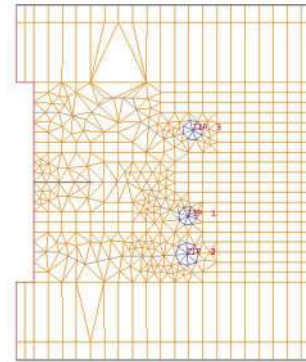


**Figure 10.** Crack growth for uniformly corroded samples
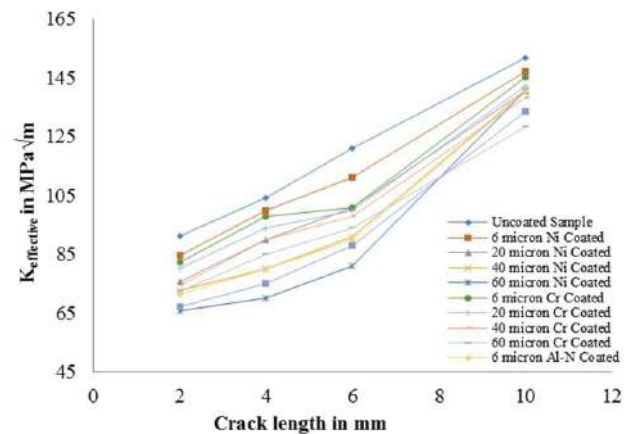


**Figure 11.** $K_{effective}$ against crack length for one year uniformly corroded steel samples
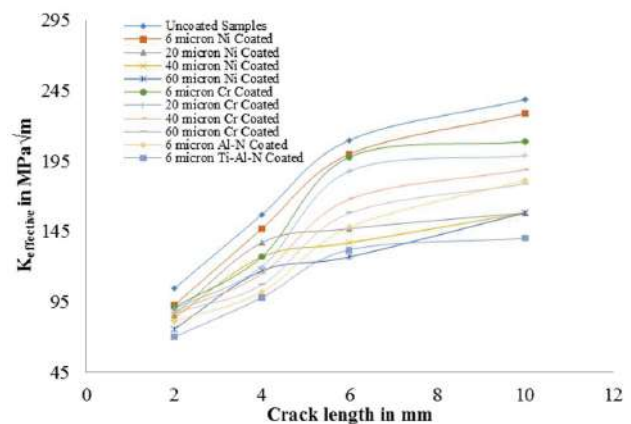


**Figure 12.** $K_{effective}$ against crack length for five year uniformly corroded aluminum samples

Figure 12 clearly explains that the increase in coating increased the corrosion resistance and indirectly reduced the $K_{effective}$ values. Particularly the 60μ coated samples

and 6μ PVD coated samples showed almost linear variations. But in the case of other uncoated and electroplated samples, a nonlinear behavior can be observed in 6μ, 20μ and 40μ samples from figure 12. The 6 Cr coated case is showing a higher order nonlinearity of stress intensity factor. The above corrosion calculations are considered in the simulation, and different cracks are grown at different regions as per figure 13. The occurrence of the first crack can influence the behavior of the other two cracks. Figure 13 also illustrates that the crack may either cut each other or the stress radiated from one crack can cause the deflection of the nearby crack.
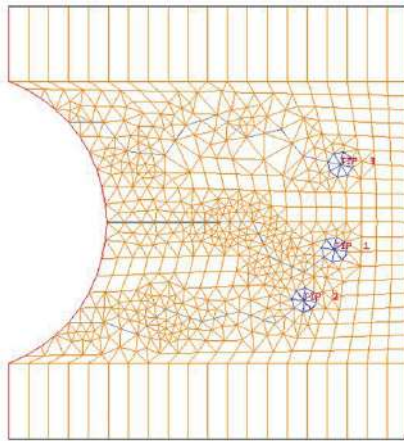


**Figure 13.** Crack growth for pitting corroded samples

The pitting corrosion results showed a decrease in $K_{effective}$ for PVD coated samples compared to electroplated samples. In pitting the $K_{effective}$ is found high compared to uniform corroded samples because of stress concentration at the pits formed. The pits formed can cause the growth of one or more cracks which may grow under the cyclic loading and corrosive environment in order to simulate this condition, multiple cracks as assumed near the pits to study the influence of pits and crack with high $K_{effective}$. Figure 14 shows a highly nonlinear behavior for uncoated and 60μ Ni electroplated samples compared to other examples the trend of which are almost linear. The increase coating thickness may lead to peeling off coating in electroplated samples.

In figure 15 an increase in the corrosion rate influenced the crack kinking and hence more $K_{effective}$ values. More importantly with an increase in crack length at around 6mm a severe shift in the values of $K_{effective}$ can be observed. The PVD coated samples and those with higher coating thickness showed a linear variation after a crack length of 6mm. As expected a lesser value of $K_{effective}$ are seen in figure 15. It can be inferred that the method of coating effects the adherence properties of the substrates and influences the corrosion resistance properties.
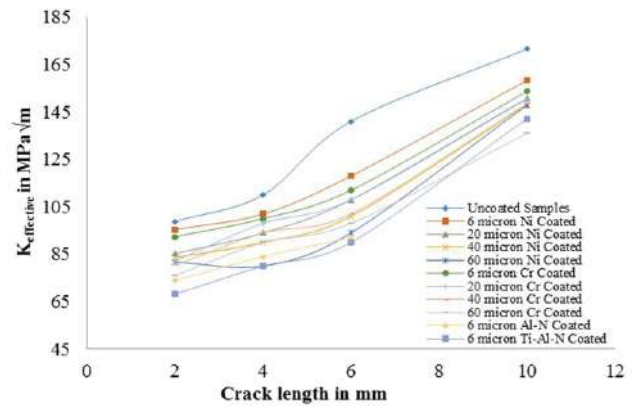


**Figure 14.** $K_{effective}$ against crack length for one year pitting corroded steel samples
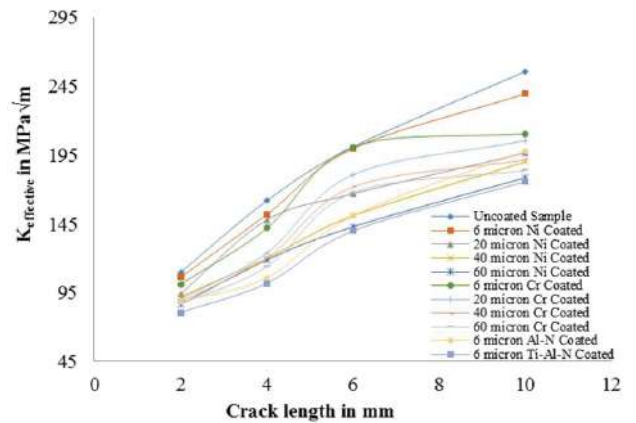


**Figure 15.** $K_{effective}$ against crack length for five year pitting corroded steel samples
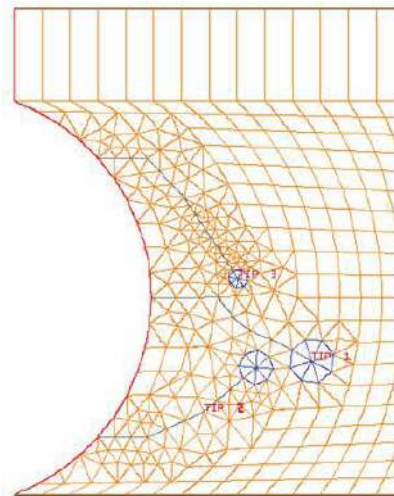


**Figure 16.** Crack growth for uniformly and pitting corroded samples.

The pitting and uniform corrosion are combined, and simulation was carried shown in figure 16 and figure 17. As per figure 16, when the multiple cracks were grown,

28
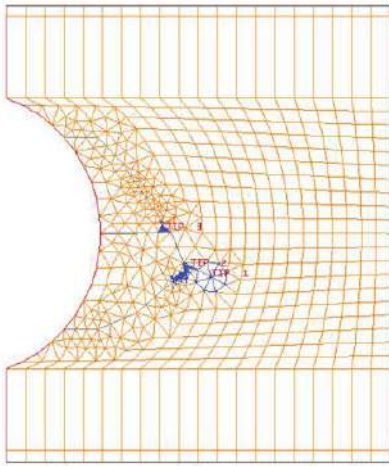
**Figure 17.** Crossing of one crack on the other

two or three cracks are seen to be meeting. It is observed in figure 17 that the two cracks followed upon their meeting, lead to chipping of part of the substrate and leading to failure of the entire structural component.

In figure 18, the combination of pitting and uniform corrosion together increased the $K_{effective}$ values compared to the total effect of uniform and pitting corrosion separately. The same phenomenon of PVD and higher coating thickness samples show a linear behavior in $K_{effective}$ values with increase in crack length. Other samples showed a nonlinear behavior as shown in figure 18.
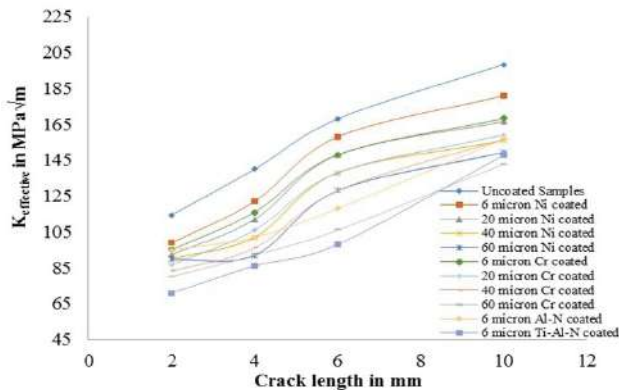


**Figure 18.** $K_{effective}$ against crack length for one year pitting and uniformly corroded steel samples

Increase in corrosion rate leads to more reduction in thickness of samples in combined corrosion phenomenon from figure 19. A rise in $K_{effective}$ values can be found because of the combined corrosion phenomenon. The PVD and higher coating thickness samples showed almost non-linear behavior. In case of other coated samples showed a highly nonlinear behavior at 6mm crack length and 10mm crack length. The kinking of crack is drastic with a reduction in thickness, and $K_{effective}$ values are affected, and the

same is illustrated using figure 19.
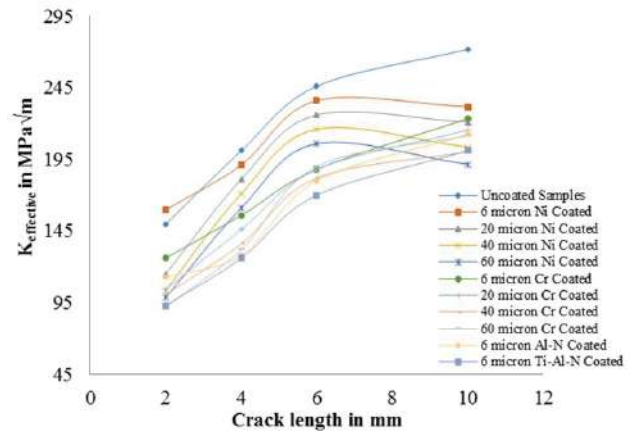


**Figure 19.** $K_{effective}$ against crack length for five year pitting and uniformly corroded steel samples

In the case of electroplated aluminum samples, the behavior of $K_{effective}$ values was different from figure 20. Compared to uncoated and higher coating thickness samples the 6μ Ni coated samples showed increased $K_{effective}$ values because of reduction in thickness. The coated samples showed a linear behavior compared to uncoated cases which are showing highly nonlinear and is as observed in figure 20.
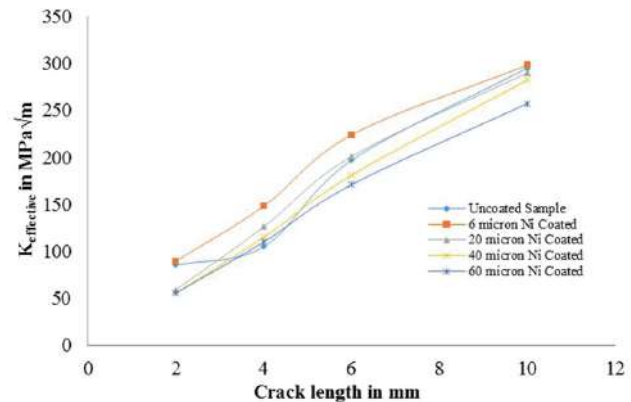


**Figure 20.** $K_{effective}$ against crack length for one year uniformly corroded aluminum samples

Further increase in corrosion rate result increased the $K_{effective}$ values as per figure 21. The uncoated samples showed a highly nonlinear behavior with a drastic increase in $K_{effective}$ values with increase in crack length. Other samples showed almost a linear behavior except 6μ Ni coated samples showed high $K_{effective}$ values.

As for the pitting corrosion of aluminum coated samples, there is increase in corrosion resistance due to the increase in coating thickness. It is shown in figure 22. All the coated and uncoated samples showed a drastic in-

29

crease K$_{effective}$ values with increase in crack length.
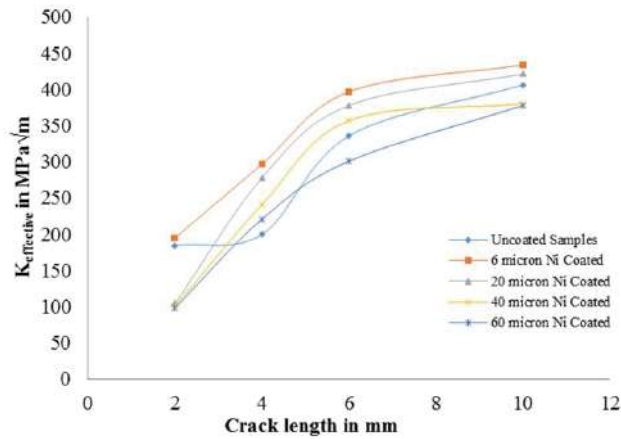


**Figure 21.** K$_{effective}$ against crack length for five year uniformly corroded aluminum samples
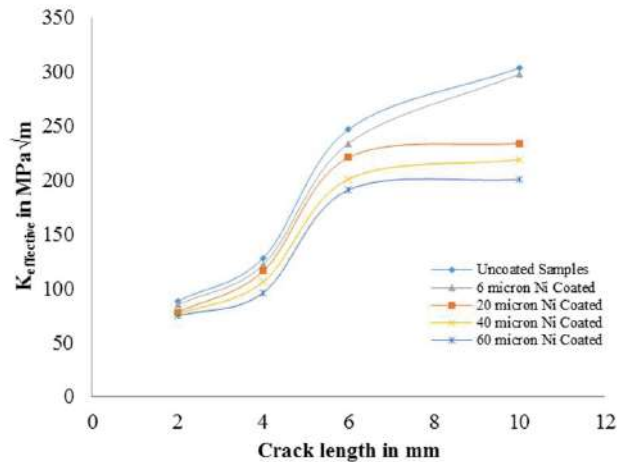


**Figure 22.** K$_{effective}$ against crack length for one year pitting corroded aluminum samples

Figure 23 shows that an increase in corrosion rate will raisethe the Keffective values. A sudden rise in K$_{effective}$ values can be observed in figure 23 near or around a crack length of 6mm. When the pit depth is increased, and stress around are also increased and with the introduction of crack the K$_{effective}$ values are shooting up as per figure 23.

In the combined case of pitting and uniform corrosion, the case of 6μ Ni coated samples showed an increase in K$_{effective}$ values and i8s shown in figure 24. Compared to pitting corrosion the uniform corrosion is dominating in corrosion rate by causing the reduction in thickness.

Therefore, compared to other samples the 6μ Ni coated samples shows a increased K$_{effective}$ values along with an increase in corrosion rate.
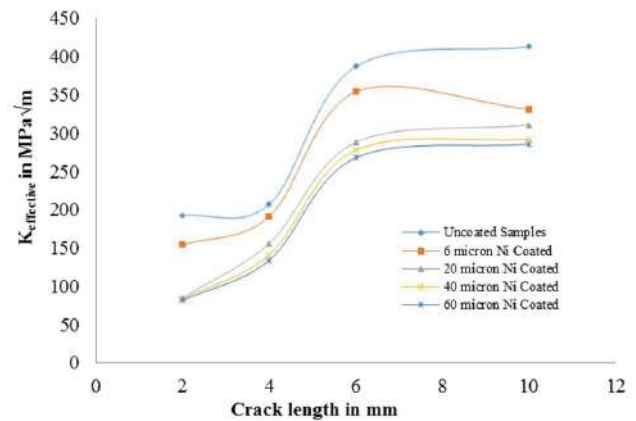


**Figure 23.** K$_{effective}$ against crack length for five year pitting corroded aluminum samples
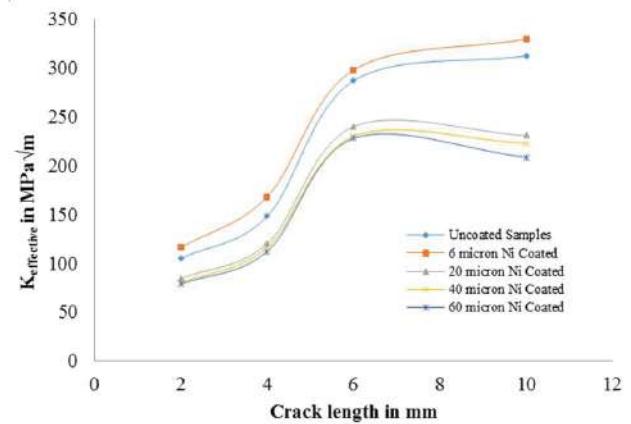


**Figure 24.** K$_{effective}$ against crack length for one year pitting and uniformly corroded aluminum samples

Figure 25 shows an increase in corrosion rate triggering a drastic increase in K$_{effective}$ values. The 6μ Ni coated samples showed a linear increase of K$_{effective}$ values with increase crack length. The uncoated samples and higher coating thickness samples showed a nonlinear behavior at 4mm and 6mm crack length. The pitting depth is influencing the behavior at a certain crack lengths and is shown in figure 25.

Fatigue analysis was performed for estimating the number of cycles against corrosion years for coated and uncoated samples of steel and aluminum. The analysis was performed by considering the effects of uniform, pitting and uniform and pitting together through figures 26-31. Figure 26 shows a number of cycles for different coated components, from the figure the uncoated samples shows a less number of cycles. The increase in coating thickness increased the corrosion resistance and increased the number of cycles.
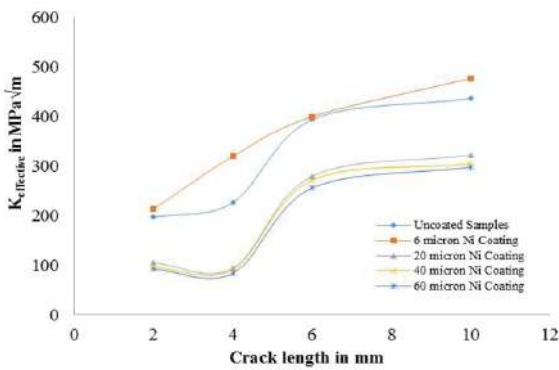
**Figure 25.** K$_{effective}$ against crack length for five years pitting and uniformly corroded aluminum samples
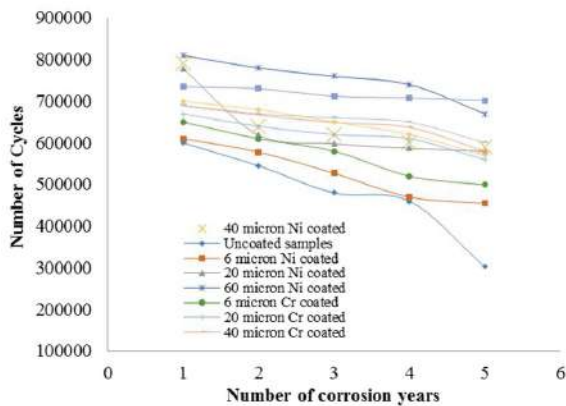


**Figure 26.** Number of cycles against corrosion years for uniformly corroded steel samples

In pitting corrosion even though the uncoated samples showed less number of cycles, other coated samples showed a different behaviors. The number cycles decreased with increase in corrosion years, but 6μ and 60μ Ni coated samples showed a different behavior with increasing the number of cycles at certain and then reducing as per figure 27.
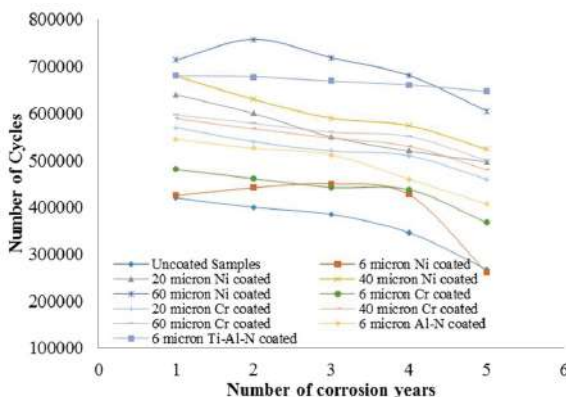


**Figure 27.** Number of cycles against corrosion years for pitting corroded steel samples

In figure 28 the combined corrosion phenomenon showed a decreased number of cycles with the increase in corrosion years. The 60μ Cr coated samples showed a reduction in a number of cycles for a three year duration of corrosion. Although increase in coating thickness increases the corrosion resistance, there is a decrease in the coating toughness and the number of cycles.
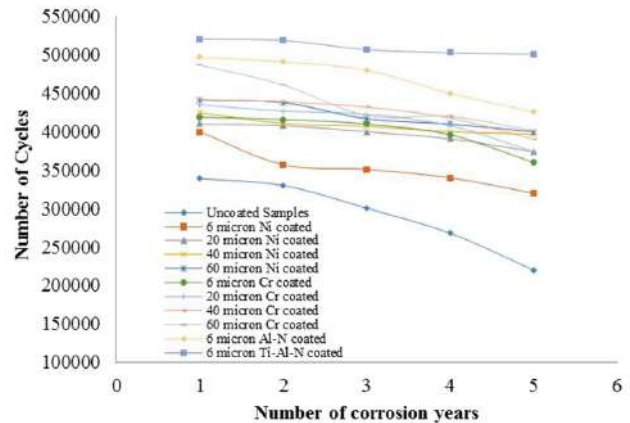


**Figure 28.** Number of cycles against corrosion years for pitting and uniformly corroded steel samples

For aluminium coated samples, there is increase in a number of cycles for an increase in coating thickness except for 6μ Ni coated samples as per figure 29. The increase in corrosion rate on the 6μ Ni coated samples result in reducing the number of cycles.
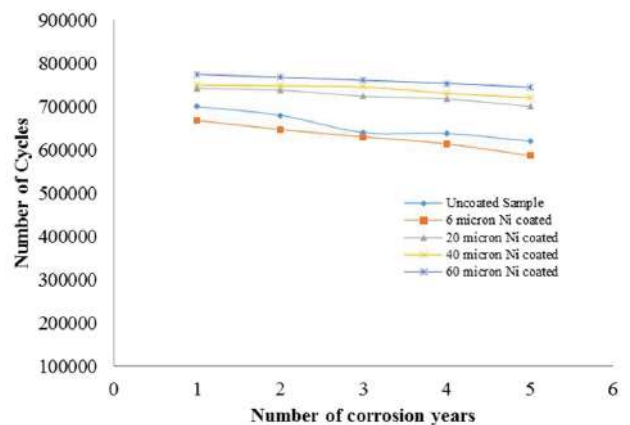


**Figure 29.** Number of cycles against corrosion years for uniformly corroded aluminium samples

In the case of pitting corrosion of aluminum samples, the uncoated sample showed an increase in a number of cycles and again decreased from figure 30. The pit depth is effecting the performance of the crack, and the number of cycles is found diminished.

31
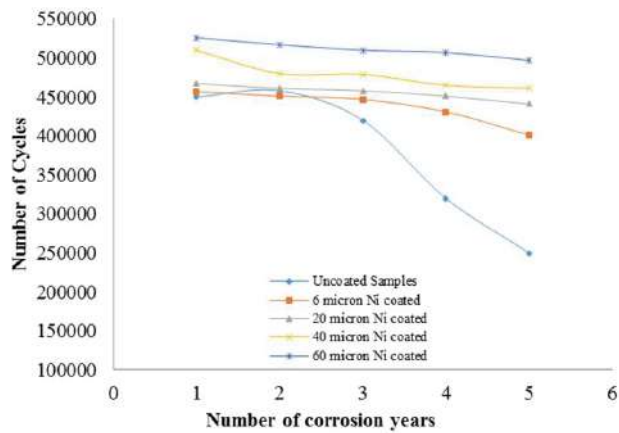
**Figure 30.** Number of cycles against corrosion years for pitting corroded steel samples

The combined effect of corrosion on aluminum coated samples did not affect much on coated samples as per figure 31. The increase in coating thickness increased the corrosion resistance and increased the number of cycles.
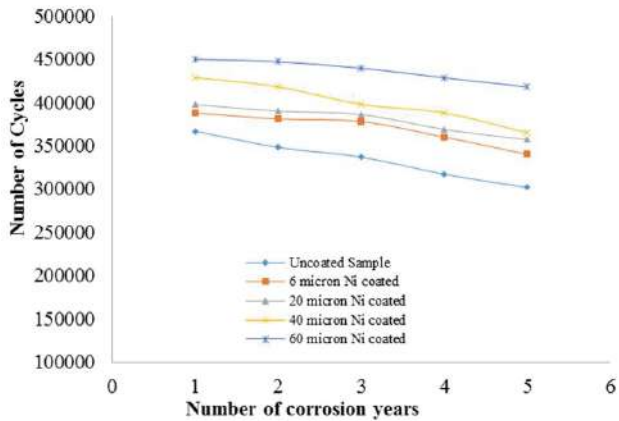


**Figure 31.** Number of cycles against corrosion years for pitting and uniformly corroded aluminum samples

The elevation of coating thickness is important for the improvement of performance of structures in severe marine environment. The most important property is toughness of coating in different conditions. For measuring this, an indentation testing is carried out for a different range of loads varying in steps of 10N, 50N, 200N, 500N and 1250 at room temperature for corroded and uncorroded samples. The SEM analysis is done for all coated sample and fracture toughness of all coating is compared. Equation (4) is used for determining the fracture toughness and found that PVD coated samples of Al-N and Ti-Al-N samples showed better fracture toughness values compared to electroplated samples. Later the uncorroded and corroded samples were compared for analysis. In figure 32 the

uncorroded Ni-coated steel sample showed more cracks compared to Cr coated samples.
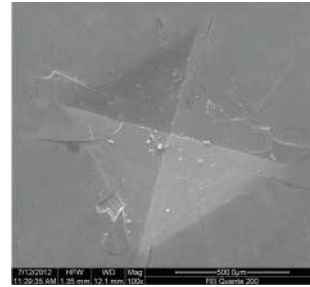


**Figure 32.** SEM image of uncorroded Ni-coated steel samples
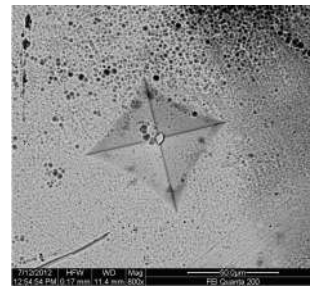


**Figure 33.** SEM image of corroded Ti-Al-N coated steel samples

The Ti-Al-N samples from figure 33 showed no cracks which indirectly increased the fracture toughness of the coating.
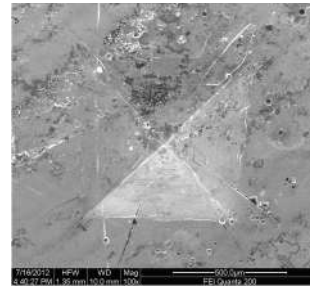


**Figure 34.** SEM image of corroded Ni-coated steel samples
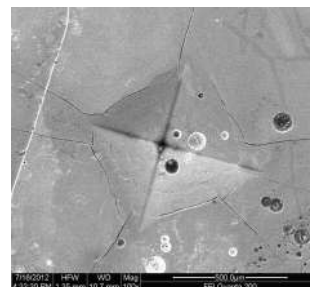


**Figure 35.** SEM image of corroded Cr coated steel samples
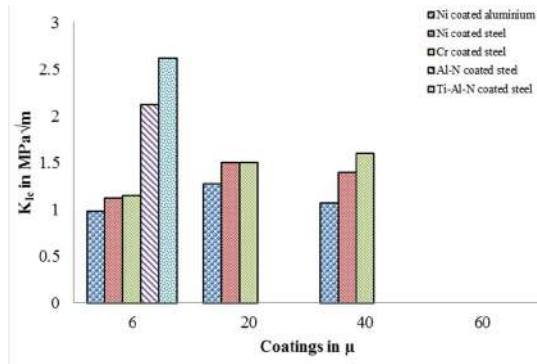
**Figure 36.** $K_{Ic}$ against coating thickness for uncorroded steel and aluminum

Later the indentation near the pitting was conducted and found that a decrease in fracture toughness with an increase of some cracks. It is shown in figure 36. The increase in some cracks was due to micro pits formed around the main pitted area. Comparatively, Cr coated samples showed less number of cracks due to an increase in corrosion resistance as per figure 37.

Though the increase in coating thickness is decreasing the rate of corrosion, it is affecting the fracture toughness of the coating. Due to the increase in coating thickness, the residual stress is increased and is seen from figure 38. This phenomena indirectly affects the coating toughness with multiple cracks. Similar behavior can be observed in 60μ Ni coated aluminum samples. Figure 38 shows the chipping of the coating due to poor adherence.
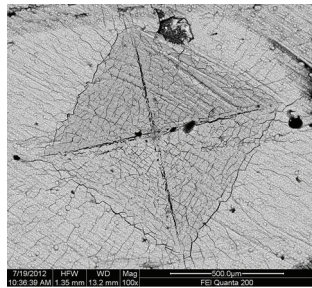


**Figure 37.** SEM image of corroded 60μ Cr coated steel samples
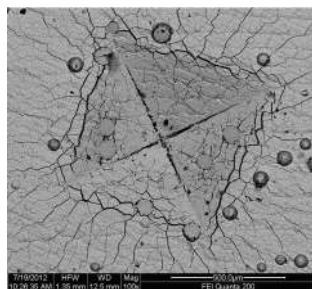


**Figure 38.** SEM image of corroded 60μ Ni coated aluminum samples
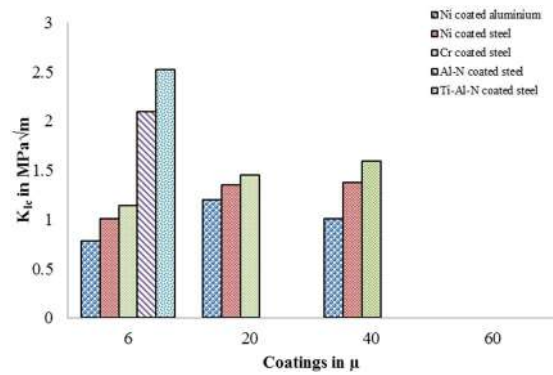


**Figure 39.** $K_{Ic}$ against coating thickness for uncorroded steel and aluminum

Figure 39 shows higher fracture toughness values are seen for PVD coated samples compared to electroplated Ni and Cr samples.

## 5. Conclusion

In the present study, the samples of high strength steel were coated with different coating methods like electroplating of Ni and Cr and PVD coating by Al-N and nano crystalline Ti-Al-N. The aluminum samples were coated with electroplating of Ni. All samples of steel and aluminium were tested by potentiodynamic polarization by ASTM G-59 and weight loss test by ASTM G-39. Following were concluded

※ Pitting and uniform corrosion on high strength steel showed that PVD coated nano crystalline Ti-Al-N and Al-N coated samples showed an excellent corrosion resistance property compared to Ni and Cr electroplated samples. 6μ of PVD coated samples showed good results compared to 20μ, 40μ and 60μ electroplated samples. Therefore, the method of coating along with coating thickness affects the performance of structural materials.

※ In pitting corrosion of Ni-coated aluminum samples increase with coating thickness. It means an increase in corrosion resistance. But in uniform corrosion due to deposition of salt on the surface of Ni-coated aluminum decreases the corrosion resistance.

※ $K_{effective}$ values are found very high for combined corrosion rate of uniform and pitting, compared to individual pitting and uniform corrosion rate.

※ Growing of multiple cracks near the corroded area showed a possibility of the crossing of cracks. Such phenomena are demonstrated using simulation.

※ Fatigue crack growth analysis showed the decrease in a number of cycles for combined corrosion rate of uniform and pitting, compared to individual pitting and uniform corrosion rate. The coating thickness and methods of coating affected the fatigue crack growth life of the samples.

※ Indentation tests showed that PVD coated samples were better in fracture toughness than electroplated samples. This is relevant for both cases of before and after corrosion.

**Author Contributions**

It is the PhD work of the first author. He is strong in experimental works and has good exposure to numerical and computer simulations. The second author is the research guide of Dr Manjunath.

**References**

[ 1 ] P. V. Petroyiannis, Al. Th. Kermanidis, P. Papanikos, Sp. G. Pantelakis, Corrosion-induced hydrogen embrittlement of 2024 and 6013 aluminum alloys, Theoretical and Applied Fracture Mechanics, 2004, 41, 173–183.

[ 2 ] Sp. G. Pantelakis, P. G. Maglaras, Ch. Alk. Apostolopoulos, Tensile and energy density properties of 2024, 6013, 8090 and 2091 aircraft aluminum alloy after corrosion exposure, Theoretical and Applied Fracture Mechanics, 2000, 33, 117-134.

[ 3 ] D. Birchon, The use and abuse of materials in ocean engineering, Proceedings of the Institution of Mechanical Engineers,1970, 24, 185.

[ 4 ] D. G. Harlow and R. P. Wei, A probability model for the growth of corrosion pits in aluminum alloy induced by constituent particles, Engineering Fracture Mechanics,1998, 59, 305-325.

[ 5 ] M Ramana Pidaparti, S. Appajoysula Rao, Analysis of pits induced stresses due to metal corrosion, Corrosion Science, 2008, 50, 1932-1938.

[ 6 ] T. G. Gooch and G. S. Booth, Corrosion fatigue of offshore structures, Metal Science,1979, 402-410.

[ 7 ] S. P. Lynch, Failures of structures and components by environmentally assisted cracking, Engineering Failure Analysis, 1994, 1(2), 77-90.

[ 8 ] Torgeir Moan, Efren Ayala-Uraga, Reliability-based assessment of deteriorating ship structures operating in multiple sea loading climates, Reliability Engineering and System Safety, 2008, 93, 433-446.

[ 9 ] Franc2d Users manual. www.cfg.cornell.edu.

[10] A. Dale Cope, S. Patrick Johnson, Angela Trego, and J. Doug West, Analytical framework for the assessment of corrosion and fatigue in fuselage lap joint, (1998) Boeing Information, Space and Defence systems, Wichita, Kansas 627277 USA. http://tregoengineering.com/PDF_Papers/afcp1998_anal_meth_dadT.pdf

[11] P. Richard Gangloff. Environmental cracking - corrosion fatigue. http://www.virginia.edu/ms/faculty/gangloffASTM

[12] Domenico "Nico" Quaranta, FRANC2D/L crack growth users guide, 2011, Revision 1.5.5.

[13] ASTM G-59 standard test method for conducting potentiodynamic polarization resistance measurements.

[14] ASTM G-31 Standard Practice for laboratory immersion corrosion testing of metals.

[15] J. Lesage, A. Roman, and D. Chicot. Indentation tests determine the fracture toughness of nickel-phosphorus coatings. Surface and Coatings Technology , 2002, 5, 161-168.

[16] B. Zaid, D. Saidi, A. Benzaid, S. Hadji. Effects of pH and chloride concentration on pitting corrosion of AA6061aluminum alloy. Corrosion Science, 2008, 50, 1841–1847.

[17] Hiroki Tamura, The role of rusts in corrosion and corrosion protection of iron and steel, Corrosion Science, 2008, 50,1872-1883.

[18] Ramana M. Pidaparti, Babak Seyed Aghazadeh, Angela Whitfield, A. S. Rao and Gerald P. Mercier. Classification of corrosion defects in Ni-Al bronze through image analysis. Corrosion Science, 2010, 52, 3661-3666.

[19] Allachi. H, Chaouket. F, Draoui. K. Protection against corrosion in marine environments of AA6060 aluminum alloy by cerium chlorides. Journal of Alloys and Compounds, 2010, 491, 223-229.

[20] Park Y I. Time-dependent risk assessment of aging ships. A Doctoral thesis submitted to Pusan State University on February 2004.

[21] Paik J K and Kim D K. Advanced method for the development of an empirical model to predict time-dependent corrosion wastage. Corrosion Science, 2012, 63, 51–58.

[22] Mohd Hairil Mohd, Do Kyun Kim, Dong Woo Kim, and Jeom Kee Paik. A time-variant corrosion wastage model for subsea gas pipelines. Available online from 18 March 2013.

[22] Manjunath G L and Surendran S. Effect of mono and composite coating on dynamic fracture toughness of metals at different temperatures. Composite Part B. Accepted on 11/03/2013.

**ARTICLE**

# Influence of Moonpool on the Total Resistance of a Drillship by the Effect of Water Motions inside the Moonpool

**Sivabalan Ponnappan   Surendran Sankunny***

Department of Ocean Engineering, Indian Institute of Technology Madras, Chennai, India.

| ARTICLE INFO | ABSTRACT |
|---|---|
| | Moonpools are openings right through the hull from continuous deck to bottom of the ship, allowing equipment or mini-submarines to be put into the water at a location on the vessel with minimum ship motion. Open moonpools in a drillship are causing additional resistance when the ship is in forward speed. It was shown that the water inside the moonpool started to oscillate at forward speed. The water mass in the moonpool is subjected to sloshing and piston modes. The vertical motion is piston mode and the longitudinal one is called as sloshing mode. This water particle motion inside the moonpool is mainly depended on the geometry, moonpool depth, and encountered wave frequency. Out of this, moonpool geometry is one of the key factors for the performance of the moonpool. The varying cross-section geometry is one of the practically possible and economically feasible solutions to reduce the oscillation to a considerable level is attempted in this paper. Also the resistance caused by the moonpool and the free surface generated around the hull is investigated with the use of computer simulation. |

## 1. Introduction

A moonpool is meant for access to underwater part from onboard ship. It is located mostly at the midship region of the drillship for under water operations either in square or rectangular in shape.In drillship, these openings are used for supply the raiser and other drilling equipment through it.This drillship moonpool is mainly subjected to two types of motions of water mass inside the column namely, piston mode and sloshing mode. The piston mode is a type of water particle motion where the water particles can be seen as a "plug" which oscillates in the vertical direction. In sloshing mode the movement of water plugs in the horizontal direction and makes a standing wave effect on the side wall of the moonpool. This piston and sloshing mode play a major role in vessel's surge and heave motion while the drill ship in operation/transit and its lead to a larger quantity of green water on the weather deck. In the case of rectangular moonpool the dominating mode is sloshing where as in square moonpool the piston mode of oscillation is the dominant one. Because of this water motion inside the moonpool the drillship regular activities may be affected. Also this water motion is the reason for a large quantity of sea water can enter on to the continuous deck of the vessel. If this quantity of water added with the green water at the deck because of the waves then the net effect

*Corresponding Author:*

*Surendran Sankunny,*

*Department of Ocean Engineering, Indian Institute of Technology Madras, Chennai, India* 600036

*Email: sur@iitm.ac.in.*

may be cause critical situation of the vessel. Also this water entry leads to the down time period of the drillship, because the crew members working on the drillship feel instability over the deck. Therefore this entry of water to the deck should be minimized to better performance of the drillship.This water motion inside the moonpool also increases the drillship resistance, when the ship is in transit condition. The moonpool opening can be close during the transit by hatch cover, but any failure happened in the operation of the hatch cover leads to stop the drillship operation. This may cause major economic loss to the company, therefore most of the transit the drillship hatch cover in open condition.

In regular moonpool geometry the water motion inside the moonpool when the drillship in operation mode is a considerable level, it further increases when the ship is in transit condition. This led to a number of studies in changing the moonpool geometry. Some of the studies are discussed here.

Moonpool hydrodynamics and the mathematical model formulated for relative water motion inside the moonpool. In both the numerical and experimental study the influence of the damping mechanism was also evaluated [1]. The numerical simulation of the free surface flow around the VLCC hull form with the use of potential flow code and viscous flow finite volume code and compared the same with the available results. The geometry of the moonpool is one of the important parameter in the case of the formation of vortices[2]. The experimental research conducted on the behaviour of the water column oscillations in different shapes of moonpool and its effects on the vessel motion. The author observed that the flow inside the moonpool mainly depended on the shape of the moonpool [3]. The flow inside the moonpool is like turbulent in nature, also the aft end of the drillship. To simulate the free surface around the hull a suitable model considered as Explicit Algebraic Stress Model (EASM) by Gatski and Speziale [4]. The water motion inside the moonpool will cause the resonance when it is at a critical level. The different levels of experiments conducted in moonpool with different motion minimizing attachments to reduce the free surface elevation inside the moonpool. The authors also attempted with a varying cross section of moonpool along the depth of the ship to reduce the water motions[5].

The experimental and numerical study of resistance and flow field was carried out in KVLCC2 hull. The EASM and SST turbulence model were used in a numerical study. The results of both the model have good agreement with the experimental study. Also, the detected outputs from turbulence models in resistance, sinkage, trim, and the free surface are found to be good[6]. The overall resis-

tance of a ship can be divided into two as wave resistance and viscous resistance[7]. Out of these two resistance part, the drillship with moonpool does not affect the wave resistance, but it affects the viscous pressure resistance due to pressure imbalance generated by the moonpool. The theoretical formulas derived for both the piston mode and sloshing mode natural frequency of moonpool in two dimensional and three-dimensional cases using linearized potential flow theory. In this study, the author formulated the free surface shape for both the piston and sloshing mode[8].

Moonpool resonant oscillations are initiated by vortices that start at the upstream bottom end of the moonpool when the drillship in forward speed condition. The model test on moonpool of the drillship with different length to breadth ratio and studied the correlation between the shape of moonpool and increase of resistance. The authors arrived at the variation of free surface elevation inside moonpool according to the ratio of draft to moonpool breadth [9]. The present study mainly on the changing the moonpool geometry by introducing cut-out angles in moonpool and the performance is compared with the zero cut-out angle moonpool. The cut-out moonpools are otherwise called the varying cross-section moonpool because its area gradually decreases from bottom to top. This decrement decreases the water motion inside the moonpool to a considerable level both in operation and transit mode of the drillship.  The performance of the cut-out moonpools is comparatively good than the zero cut-out angle moonpool. In this study, two different cut-out moonpools (20 degrees and 30 degrees) are used for the computer simulations for the study of free surface and the resistance.

## 2. Moonpool Modeling

The computer simulation is done by the use of SHIP-FLOW package for different Froude numbers and different draft of the drillship. The total resistance coefficient, free surface around the hull, trim and sinkage are found from the computer simulation. The body plan of the drillship and the main particulars of drillship are given in Figure 1 and Table 1 respectively. A full-length drillship is used for the computer simulation.
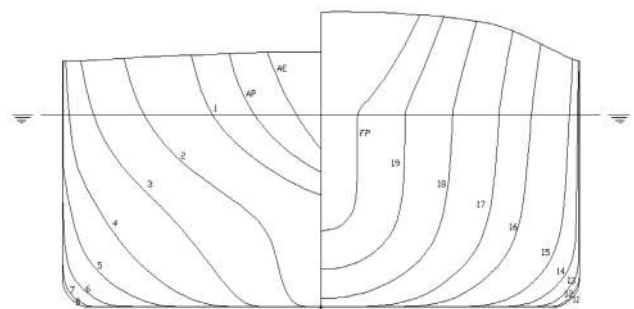


**Figure 1.** Body plan

All the iteration the same hull is used with different moonpool configurations. All the rectangular, 20-degree cut-out moonpool and 30-degree cut-out moonpool are placed at the midship area of the hull. Clear views of cut-out moonpools and rectangular moonpool are given in Figure 2.

**Table 1.** Principal dimensions of the ship

| Specification | Value |
|---|---|
| Length (LOA) (m) | 292 |
| Length(LBP) (m) | 280 |
| Breadth (m) | 50 |
| Draft (m) | 16.5 |
| Depth (m) | 25.48 |
| Displacement (ton) | 1,94,156 |

In cut-out moonpool case the cut-out is given in the aft end of the moonpool and the other end (forward end) is simply a vertical wall. This cut-out angle gradually decreases the cross-sectional area of the moonpool from bottom to top and the moonpool like a varying cross-section moonpool.
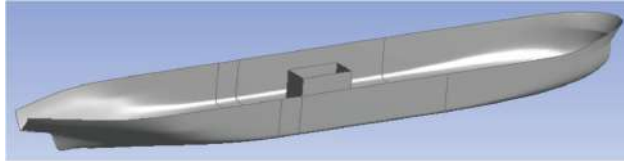


**Figure 2.**(a) Drillship hull with a rectangular moonpool
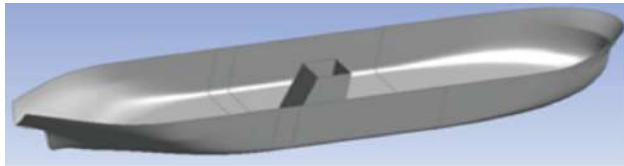


**Figure 2.**(b) Drillship hull with 20-degree cut-out moonpool
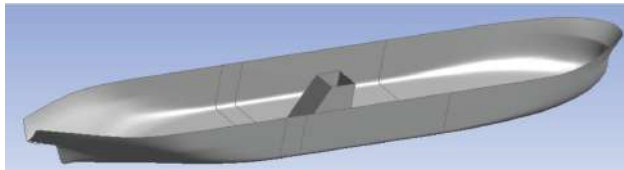


**Figure 2.**(c) Drillship hull with 30-degree cut-out moonpool

## 3. Computer Simulation

### 3.1 Shipflow Theory

In the present study, SHIPFLOW package is used for the computational study. The features of the SHIPFLOW CFD code has discussed here. In this, the solver solves the flow problem in a zonal approach. In an overall view,

it divides the object into three zones with three different solution approaches. Zone 1 uses the potential flow solver with Rankine source panel method. In the potential flow method, the SHIPFLOW code can be run in both linear and non-linear mode. It solves the forward portion of the ship hull.

$$\nabla^2 \phi = \frac{\partial^2 \phi}{\partial x^2} + \frac{\partial^2 \phi}{\partial y^2} + \frac{\partial^2 \phi}{\partial z^2} = 0 \qquad (1)$$

In Zone 2 in SHIPFLOW, the boundary layer is computed using a momentum-integral method. It is based on streamlines, which are automatically traced from the potential-flow solution.

In Zone 3 the governing equations are the Reynolds-Averaged Navier-Stokes (RANS) equations, obtained by averaging the time-dependent Navier-Stokes equations over the entire length and time scales of the turbulent fluctuations. It solves the aft end of the ship hull by turbulent flow solver.

$$\frac{\partial}{\partial t}(\rho) + \frac{\partial}{\partial x_i}(\rho u_i) = 0 \qquad (2)$$

$$\frac{\partial}{\partial t}(\rho u_i) + \frac{\partial}{\partial x_i}(\rho u_i u_j) =$$
$$-\frac{\partial p}{\partial x_i} + \frac{\partial}{\partial x_i}(-\rho \overline{u'_i u'_j}) + \qquad (3)$$
$$\frac{\partial}{\partial x_j}[\mu(\frac{\partial u_i}{\partial x_j} + \frac{\partial u_j}{\partial x_i} - \frac{2}{3}\delta_{ij}\frac{\partial u_l}{\partial x_l}]$$

SHIPFLOW software consists of a number of compact modules like XMESH, XPAN, XBOUND, and XGRID, each briefly discussed here.

XMESH is the mesh generator that creates panels for the hull and the free surface for the potential flow solver, XPAN. In the present study totally 7529 panels are generated for the potential flow study. XPAN is the potential flow solver. It solves the potential flow around the bodies based on a panel method and using the mesh generated by XMESH. XPAN can compute the wave resistance, wave pattern, pressure contours, and sinkage/trim. The result from XPAN is stored in a database file required to run the XBOUND module.

XBOUND is the module that deals with the turbulent boundary layer but is also capable of computing the laminar boundary layer. BOUND creates a database file required to execute XCHAP.

XGRID creates the grid used in viscous computations in XCHAP. With XGRID it is possible to create grids for ship or submarine hulls.

XCHAP is a module that solves Reynolds Averaged Navier-Stokes equations using one of several available turbulence models (EASM, k-ω BSL, k-ω SST). The Explicit Algebraic Stress model (EASM) used in the turbulent flow analysis. The total resistance can be computed by combining the results from XPAN, XBOUND, and XCHAP.

In the present study the free surface elevation inside the moonpool, the total resistance act on the drillship and the free surface around the hull are simulated for different Froude numbers in all different moonpool configurations.

### 3.2 Free surface Wave Eevation

The free surface wave elevation inside the moonpool may be any one of the following condition. i) during transit condition in the drilling location, ii) wave heading during stationary condition. The oscillations inside the moonpool initiated during forward speed condition by vortices, formed at the leading end of the moonpool. Because of the flow separation of the shear layer at the bottom of the hull nearby forward end of the moonpool. These oscillations increase the resistance also the deck wetness.

In the case of cut-out moonpool the free surface elevation considerably controlled when it is compared with the rectangular moonpool. The oscillations inside the moonpool are suppressed by the tapered wall of the moonpool. In rectangular moonpool this oscillation like a standing wave on the side walls. The effect of the oscillations inside the moonpool creates noise and pressure on the structure.

The amplitude of the free surface elevation mainly depends on the speed of the drillship and geometry when the ship is in forward speed condition. The pressure acting on the moonpool wall is directly proportional to the forward speed. This pressure drops when the velocity increases, this is due to the free surface oscillating frequency and the shear layer oscillating frequency.

The free surface elevation from the computer simulation for the Froude number of 0.0393 is given in Figure 3.This is given along the center line of the hull along the length of the vessel. The simulation done for various Froude numbers (0.0196, 0.0393, 0.0589, 0.0785, 0.0982, 0.118, 0.137, and 0.157) with the vessel maximum loaded draft. The free surface elevation increases once the velocity increases as shown in Figure 3(a). The maximum elevation is at the aft end of the vessel.

The rectangular moonpool effect in the hull when it compared with the without moonpool hull is given in Figure 3(b). It have the maximum elevation as compared with the cut-out moonpool is given in Figure 3(c).In cut-out moonpools, the effect of the free surface has smaller difference as shown in Figure 3(d) . From Figure 3 it is clearly

mentioned that the cut-out moonpools are comparatively good in the reduction of free surface elevation by suppressing the water particle movement and act as a damper.
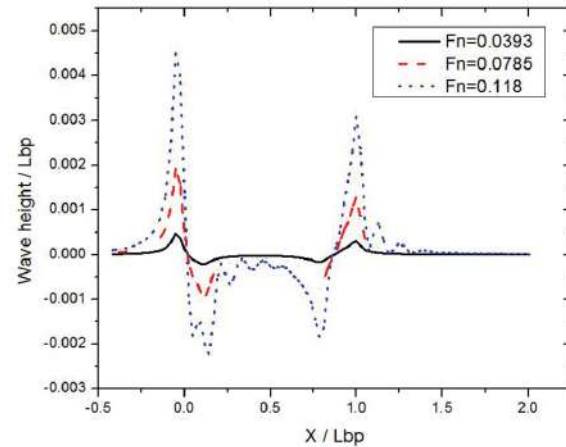


**Figure 3(a).** Free surface elevation in the bare hull
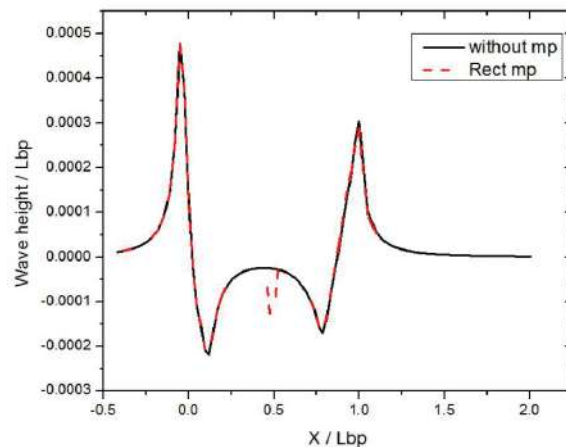


**Figure 3(b).** Free surface elevation in the rectangular moonpool
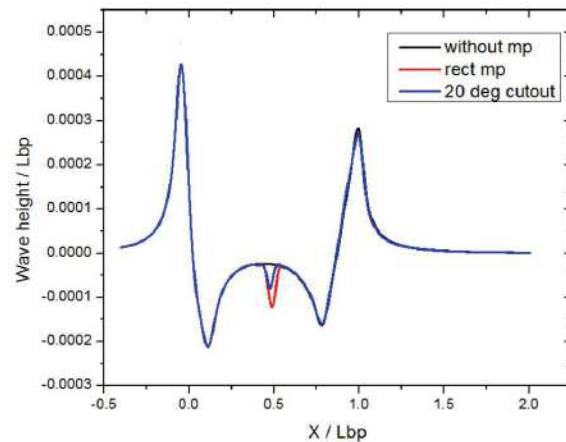


**Figure 3(c).** Free surface elevation in 20-degree cut-out moonpool
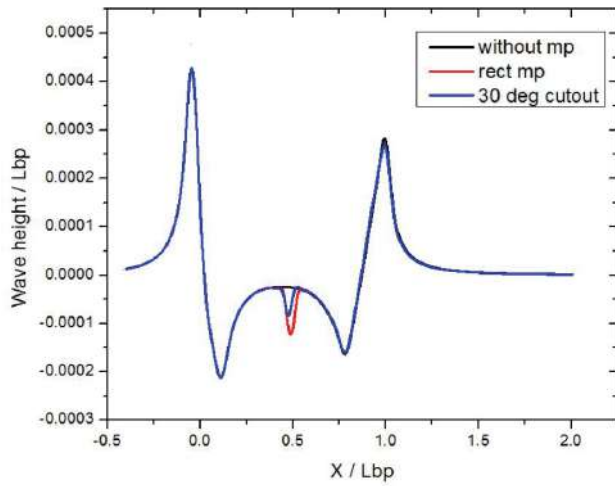
**Figure 3(d).** Free surface elevation in 30-degree cut-out moonpool

### 3.3 Pressure on the Hull

The pressure distribution over the bow part of the drillship from XPAN at Froude number 0.0393 is given in Figure 4.The pressure distribution is given in the form of pressure coefficient, it can be found panel wise. This pressure distribution over the hull is used for the calculation of wave resistance. The total pressure acting along the hull is directly proportional to the wetted surface area, velocity, and density of salt water. The pressure coefficient is simulated using the panel method. The pressure distribution over the hull is used to find the critical regions. High fluctuation of pressure along the waterline represents the wave crest and the trough. The drillship has higher block coefficient like tanker vessel, the wave making resistance/wave breaking resistance have a higher value near the forward shoulder part of the vessel. That can be found by pressure integration of over the hull.
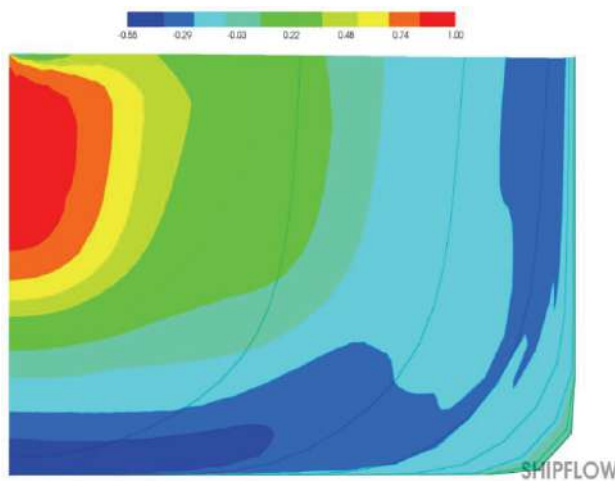


**Figure 4.** Pressure distribution over the bulbous bow

### 3.4 Free Surface Around the Hull

The free surface around the drillship hull without moonpool and 20-degree cut-out moonpool at Froude number 0.0393 is given in Figure 5(a) and 5(b) respectively.
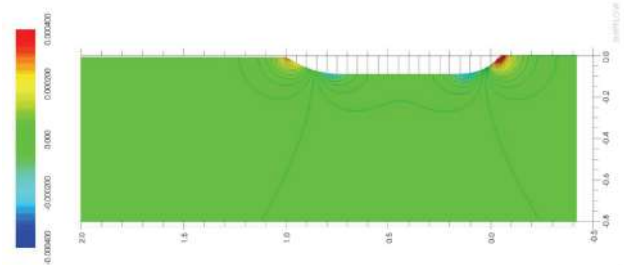


**Figure 5(a).** Free surface around a bare hull
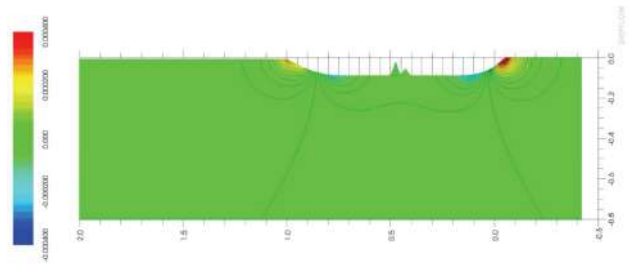


**Figure 5(b).** Free surface around the drillship hull with 20-degree cut-out moonpool

### 3.5 Total Resistance

The total resistance coefficient ($C_T$) from the simulation is the combination of wave resistance coefficient ($C_w$), viscous resistance coefficient ($C_v$). In the viscous part; frictional resistance coefficient ($C_F$) and viscous pressure resistance coefficient ($C_{PV}$) are counted. This viscous part is added with the wave resistance part and the total resistance coefficient is evaluated.

$$C_v = C_F + C_{PV}$$
$$C_T = C_v + C_w$$

$$C_T = \frac{R_T}{0.5\rho S V^2} \tag{4}$$

The total resistance ($R_T$) of the vessels is directly proportional to the wetted surface area, the speed of the vessel and density. The total resistance of the drillship against different Froude number is plotted in Figure 6.

### 4. Conclusions

The total resistance of the drillship and the effect of free surface with different selected moonpool configurations are discussed in this paper. The computer simulation conducted for different Froude numbers in the loaded draft of the drillship. The XCHAP simulation runs up to
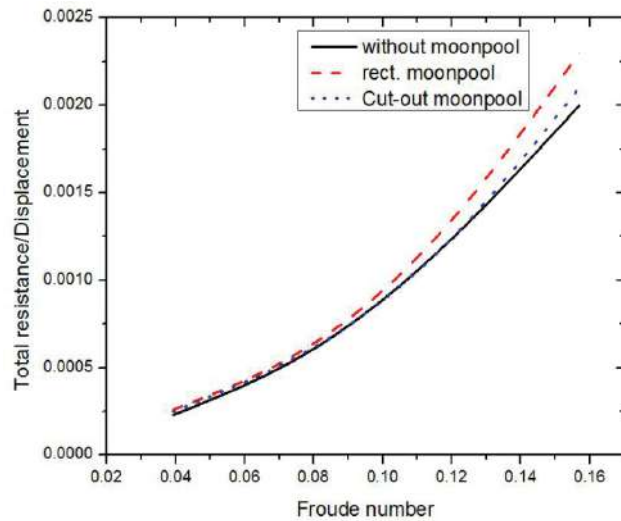
**Figure 6.** Total resistance

5000 iterations for convergence results. The moonpool with cut-out angles is good in controlling the free surface elevation inside the moonpool as compared with the rectangular moonpool. When the moonpool is open to the sea there is an increase in the resistance of ship when it is in forward speed condition. The moonpool with cut-out angle gives the resistance in between the rectangular moonpool and hull without moonpool. From the CFD simulation, it is understood that the hull with moonpool geometry disturb the flow at the bottom of the hull and increases the resistance of the ship. This increment in resistance will increase the fuel consumption of the drill-ship in transit.

## NOMENCLATURE:

| | |
|---|---|
| $\phi$ | Flow potential |
| $\upsilon$ | Kinematic viscosity (m$^{-2}$ s$^{-1}$) |
| $\rho$ | Density of water (kg m$^{-3}$) |
| $P$ | Pressure (N m$^{-2}$) |
| $F_n$ | Froude number |
| $V$ | Speed (m s$^{-1}$) |
| $S$ | Wetted surface area (m$^{-2}$) |
| $\mu$ | Dynamic viscosity (N s m$^{-2}$) |
| $X$ | Position along the length of the vessel |

## Author Contributions:

Sivabalan P. He has done this work for his Ph D. The works consisted of experimental and numerical simulations using package programmes.
Surendran S. The work discussed in the paper was done under the guidance of the second author.

## Conflict of interests:

There is no conflict of interest with any agencies/institutes or persons.

## References

[ 1 ] Aalbers AB, The water motions in a moonpool. Journal of Ocean Engineering 1984, 11(6):557-579.

[ 2 ] Ahmed Y, Guedes Soares C, Simulation of free surface flow around a VLCC hull using viscous and potential flow methods. Journal of Ocean Engineering 2009, 36, 691-696.

[ 3 ] Fukuda K., Behavior of water in vertical well with bottom opening of ship and its effects on ship-motion. Journal of the Society of Naval Architects of Japan, 1977, 141, 107-122.

[ 4 ] Gatski TB, Speziale CG, On Explicit algebraic stress models for complex turbulent flows. Journal of Fluid Mechanics 1993, 254, 59-78.

[ 5 ] Guilhem Gaillarde, Anke Cotteleer, Water motion in moonpools empirical and theoretical approach. Maritime Research Institute. Netherlands, 2005.

[ 6 ] Guo BJ, Deng GB ,Steen S, Verification and validation of numerical calculation of ship resistance and flow field of a larger tanker. Journal of Ships and Offshore Structures, 2013, 8, 3-14.

[ 7 ] Larsson L.,Raven HC, The Principles of Naval Architecture Series Ship resistance and flow, The Society of Naval Architects and Marine Engineers, 2010.

[ 8 ] Molin B, On the piston and sloshing modes in moonpools. Journal of Fluid Mechanics 2001, 430, 27-50.

[ 9 ] RianVantVeer, Tholen HJ, 'Added resistance of moonpools in calm water', Proceedings of the ASME Twenty Seventh International Conference on Offshore Mechanics and Arctic Engineering, 2008.

## ARTICLE

# A Practical Decision Making on Design of Fixed Offshore Wind Turbine Support Structure Considering Socio-economic Impact

**M Vishnu   Surendran Sankunny***

Department of Ocean Engineering, Indian Institute of Technology Madras, Chennai, India

| ARTICLE INFO | ABSTRACT |
|---|---|
| | Wind energy is considered one of the most promising alternative energy sources against the conventional fossil fuels. However, the deployment of these structures in deep-water for better power production is considered as a complex task. This also has raised the issue regarding selection of appropriate support structures for various sea conditions by considering environmental impact and carbon footprint. This paper considers a jacket like support structure as a case study for an intermediate water depth (50m). The jacket is considered to be located in North of Dutch Sea, and 100-extreme wave is applied as load condition. Here, the presented methodology provides an insight towards environmental/social impact made by the optimized designs in comparison with reference design. |

## 1. Introduction

Fixed offshore structures are one of the most commonly used offshore structures for intermediate water depths compared to monopile. These are technically feasible and economically viable in design but are complex to design in nature. This possess many challenges in designing and execution of the project. Moreover, offshore structures are designed to resist extreme wave loading but can succumb to collapse damage due to failure of multiple components members.

One major challenges faced by industry is cost effective design of structures under extreme and normal environmental conditions. For a reliable and cost effective design under extreme loads, a non-liner static structural analysis always been a significant aspect. Computer aided structural optimization can assist in designing economical

structure under various constraints like fatigue. Hence, optimization of structure has to fatigue and extreme loads under the target life. Chew et al.[1] has considered gradient based optimization and reported the importance of buckling and fatigue load constraints over the design variables. Gentils et al.[2] integrated Genetic algorithm (GA) and FEA (Finite Element Analysis) to optimize support structure under various constraints. The paper also reported the advantage of using meta-heuristic methods as compared to gradient based optimization. Gomes[3] has studied the truss optimization using particle swarm optimization (PSO)[4] based on the reported the well behavior of the algorithm.

In most cases, API and ISO codes are used to design structures under elastic and component based design[5,6]. However, Nizamani[7] suggested the advantage of system based design considering structure as a whole component.

*Corresponding Author:*

*S Surendran,*

*Department of Ocean Engineering, Indian Institute of Technology Madras, Chennai, India; Emial: sur@iitm.ac.in*

The stress re-distribution between the members can result in extended load capacity towards plastic stage based design [8]. Hence the approach proposed by Ueda et. al [9] is used in this paper by using a finite element based code, USFOS[10].

In 2007, as per major world leaders a 20% share of energy from renewable sources by 2020, by making individual targets for all EU Member States [11]. The UK targets to acquire 15% of its final energy intake from renewable sources by 2020 and to decrease $CO_2$ emissions by a minimum of 26% by 2020 and 60% by 2050 [11] and also having the best geographically varied wind resources in Europe [12]. So, it is also worth considering the social impact made by a wind energy project at various stages from manufacturing, installation and decommission stages. Lozano-Minguez et al.[12] investigated regarding the influence of environmental factors like carbon foot, noise, and vibration, water turbidity, etc. The authors also proposed the advantage of using TOPIS (Technique for Order Preference by Similarity to Ideal Solution) method as multi criteria decision making tool.

From the above literature review, the authors understand the importance of considering socio-economic impact on decision making of offshore structural designs. Hence, this paper aims to provide an analytical methodology for the selection of the most preferable fixed jacket like support structure for a typical 5 MW wind turbine in 50 m water depth. In this analysis; engineering, economics, and environmental assessment will be considered to balance the socio-economic activities of the sustainable energy sector. Figure 1 below provides sketch of offshore wind turbine (OWT) support structure under environmental loads and the methodology followed is given below Table 1.
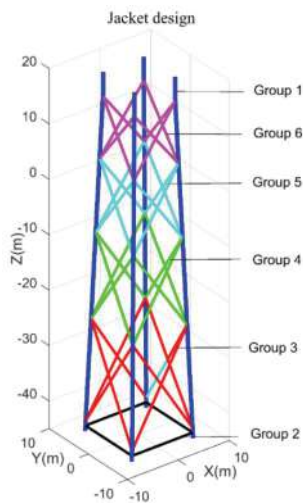


**Figure 1.** Jacket model

**Table 1.** Methodology

| Step 1 | Selection of site, loading condition and structure |
|---|---|
| Step 2 | Evaluating optimal designs under constraints |
| Step 3 | Evaluate social impact for each design |
| Step 4 | TOPIS method |

## 2. Methodology

### 2.1 Step 1: Case Study

A fixed jacket structure was proposed by Vorpahl et al.[13] was designed to support an offshore wind turbine of 5 MW capacity. The height of the jacket structure is 66m and is placed at a water depth of 50m. The location to be installed is considered as The North of Dutch Sea. The structure consists of 56 nodes and 104 beams of steel tubular cross section and used in this paper to perform structural optimization. The jacket structure is modelled using USFOS as shown below Figure 1. The tubular members of the jacket are categorized into six groups to utilize them for the structural optimization, and the cross sectional details of the groups are given Table 2. Also, the structure can work with stand loads even if one member is failed under yield conditions and the force redistribution happens to other members. This is indicated by factor referred as Reserve Strength Ratio (RSR) and considers the nonlinear static capacity of the structure [14].

$$RSR = \frac{Ultimate\ collapse\ load}{Design\ load} \qquad (1)$$

**Table 2.** Jacket reference design (continued)

| Design variable | Description | Diameter (mm) | Thickness (mm) |
|---|---|---|---|
| Group 1- Dark Blue | Leg | 1200 | 50 |
| Group 2- Red | Brace | 800 | 20 |
| Group 3- Yellow | Brace | 800 | 20 |
| Group 4-Green | Brace | 800 | 20 |
| Group 5-Cyan | Brace | 800 | 20 |
| Group 6-Blue | Brace | 800 | 20 |

The jacket material properties are given in Table 3.

#### 2.1.1 Hydrodynamic Loading

The wave environment used is based on statistical wave description. Table 4 gives the significant wave height and the hydrodynamic forces acting on the tubular members are calculated using Morison's equation [15].

As per Equation (2), the relationship between wave height and return period was formulated as:

$$H_{s,3hrs}(T_{return}) = 0.6127 \cdot \ln(x) + 7.042 \qquad (2)$$

**Table 3.** Jacket Properties

| Property | Description |
|---|---|
| Material used | Steel |
| Elastic modulus | $2.1 \times 10^5$ MPa |
| Poisson's modulus | 0.3 |
| Yield Strength | 345 MPa |
| Density | 7850 Kg/m$^3$ |
| Dead load | 350 Ton |
| X joints | 16 |
| K joints | 24 |
| T/Y joints | 16 |
| Height | 66 m |
| Mass | 608 Ton |

From the 100-year return period significant wave height, extreme design wave is calculated by the following relationship (16):

$$H_e = 1.86 H_s \tag{3}$$

For the given location, the shallow water depth allows the use of 1.86 as the factor and the loading condition shown below.

**Table 4.** Wave data

| Parameter [Unit] | Description | Value |
|---|---|---|
| $H_s,100$ [m] | Significant wave height in 100 year return period | 9.90 |
| $H_e,100$ [m] | Extreme wave height in 100 year return period | 18.41 |
| $V_{100}$ [m/s] | Mean wind speed in 100 year return period | 44.50 |
| $U_{100}$ [m/s] | Current speed in 100 year return period | 1.20 |

A typical analysis for the considered reference case and given wave leading is shown below Figure 2. The load displacement curve indicates the maximum load factor or RSR. Here the RSR is evaluated as 3.6 and is over conservative as compared to minimum prescribed values of 1.58 and 1.85 provided by API and ISO respectively. However, there seems to be lack of knowledge on target RSR values for various site and loading conditions. Also, considering target values from code based methodology for offshore oil and gas structures for wind energy system may not be feasible approach. This demands multi criteria based decision making methodology in conjunction with optimization of structures to evaluate target load factor.
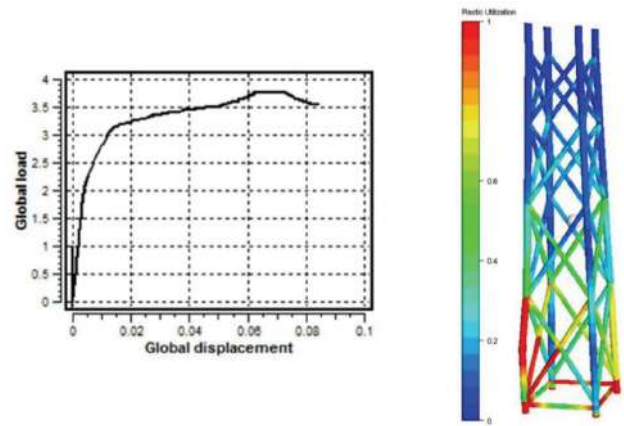


**Figure 2.** Typical load deflection curve for reference case

## 2.2 Step 2: Integrated USFOS-MATLAB Optimization

In the present study, the evolutionary approach based particle swarm optimization (PSO) algorithm proposed by Kennedy and Eberhart is considered[17]. Perez[18] and Gomes[3] reported the robustness of PSO algorithm for truss optimization. Initially, the design variable and objective functions are defined. Fitness values for each design is evaluated by integrating finite element structural analysis with PSO algorithm developed in MATLAB (Figure 3).

(a) Problem formulation

The optimization problem for minimizing structural weight with design variables, subject to sizing and ultimate collapse load factor as constraints, can be formulated as follows. The optimization problem can be formulated as given below:

Minimize jacket mass:

$$f(x) = \sum_{i=1}^{n_e} \rho_n A_n(x) l_n \tag{4}$$

Subjected to:

$$RSR \geq RSR_t \text{(varied from 1.6 to 3.2)}$$

$$x_L \leq x \leq x_U$$

RSR is the collapse load factor for given wave load. Here $x$ represents the vector of jacket member dimensions namely, diameter and thickness; $A$ is the vector of cross section area, $l$ represents the length of each member, $n_e$ represents the total number of members. This is a simplified representation of the cost function and other cost components that are incurred in the design life cycle of support structures, excluding manufacturing, installation and maintenance costs.

(b) Sizing constraints

Sizing constraints define the lower and upper bounds of

design variables as well as the geometrical relationships among the variables. They can be expressed as

$g_1 = b_{min} \leq b \leq b_{max}$

Here $b_{min}$ and $b_{max}$ are the lower and upper bounds of the design variables as shown in below Table 5.

**Table 5.** Design bounds

| Member type (Group) | Diameter bound (mm) | Thickness bound (mm) |
|---|---|---|
| Legs (1) | (600,1400) | (30,60) |
| Braces(2,3,4,5,6) | (400,800) | (10,30) |
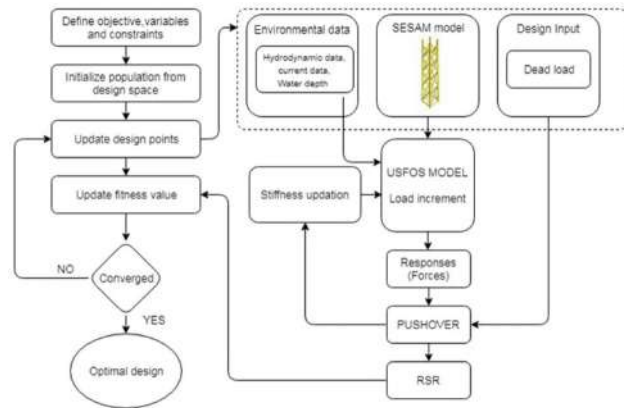


**Figure 3.** Integrated USFOS-MATLAB optimization framework

The results for the optimsation are shown in Table 6 for various target RSR values.

**Table 6.** Optimal design vs. RSR

| Mass (Ton) | RSR |
|---|---|
| 285 | 1.6 |
| 324 | 1.8 |
| 365 | 2.0 |
| 398 | 2.2 |
| 430 | 2.4 |
| 447 | 2.6 |
| 480 | 2.8 |
| 525 | 3.0 |
| 538 | 3.2 |

### 2.3 Step 3: Economic and Environmental Impact Assessment (EEIA)

This section will describe about the various environmental and social impact made by installation of jacket structure. This mainly includes the following factors:

(a) Carbon footprint

The equivalent amount of Carbon di Oxide ($CO_2$) can be expressed as following:

$$CO_2e = 270 \times N_2O + 24.5 \times CH_4 + 1.4 \times CO \qquad (5)$$

For steel structures, the emission unit per kg of total weight is 0.07, 0.04 and 0.93 g for $N_2O$, $CH_4$ and $CO$ respectively

(b) Noise and Vibration

As the machinery used is the same and the duration of the work will not vary significantly, it can be assumed that the choice of foundation will not affect the impact.

(c) Electromagnetic fields

However, it is not yet known whether the fish will suffer any consequences caused by this interaction. The choice of foundation will not, therefore, be considered as affecting the impact.

(d) Impact on birds

The choice of foundation will not affect the impact on birds.

(e) Net present value

This parameter will convert the total cost of the service life of the structure to present value.

### 2.4 Step 4: Multi Criteria based Decision Making (TOPIS)

As given in publicly available literature by Lozano-Minguez et al. [12], the basic steps of multi criteria based decision making algorithm is given below. For more information, the readers are advised to refer the above paper.

(a) Formulate initial design matrix

(b) Normalized design matrix

(c) Construct weighing matrix from experts

(d) Weighted normalized decision matrix

(e) Derived PIS and NIS

(f) Evaluate relative closeness of each solution

(g) Ranking the solution

Analysis of attributes for finding the optimal design from possible nine alternative designs, nine criteria has been considered as follows (Table 7).

**Table 7.** Description of attributes

| Sl. No | Attribute | Negative/ Positive | Value significance |
|---|---|---|---|
| 1 | Artificial reefs | Positive | Higher the better |
| 2 | Certification | Positive | 1- If certified 0.5- If not certified |
| 3 | $CO_2e$ | Negative | Lower the better |
| 4 | Depth compatibility | Negative | 1 for depth < 40 m |
| 5 | Durability | Positive | 5 for Jacket and 4 for monopile |
| 6 | Life cycle cost | Negative | CAPEX + OPEX |
| 7 | Reserve strength ratio (RSR) | Positive | Higher the better |
| 8 | Water turbidity | Negative | 2356 for jacket and 1530 for monopile |

The weights as shown in Table 8 used for the study influence the decision approaching and has been taken from experience of experts from Cranfield offshore renewable energy group[12].

**Table 8.** Weight factor for each attribute

| Attribute | 1 | 2 | 3 | 4 | 5 | 6 | 7 | 8 |
|---|---|---|---|---|---|---|---|---|
| Expert weight | 0.65 | 0.65 | 0.91 | 0.91 | 1.00 | 1.00 | 0.83 | 0.74 |

## 3. Results and Discussion

For the nine design combination corresponding to jacket based support structure, only the attribute 3, 6 and 7 are variables with no change for remaining. For evaluating the life cycle cost excluding risk expenditure, the capital cost (CAPEX) is evaluated considering 1000 € per Ton as material cost and Manufacturing cost as 400% of Material cost. For evaluating Operational cost (OPEX), it is considered as 10% of the CAPEX. However, a present worth factor should be considered to take care of the economic parameters during the life span of 20 years.

$$P_w = \frac{(1+d)^{LS}-1}{d(1+d)^{LS}} / LS \tag{6}$$

Below is tabulated results of LCC and RSR for each design index (Table 9).

**Table 9.** LCC vs. RSR for each optimal design

| Design Index | LCC ($10^6$ Euro) | RSR |
|---|---|---|
| 1 | 2.92 | 1.6 |
| 2 | 3.13 | 1.8 |
| 3 | 3.34 | 2.0 |
| 4 | 3.45 | 2.2 |
| 5 | 3.62 | 2.4 |
| 6 | 3.75 | 2.6 |
| 7 | 3.90 | 2.8 |
| 8 | 4.10 | 3.0 |
| 9 | 4.21 | 3.2 |

(a) Based on the attributes (1-8), the initial decision matrix is given below Table 10

**Table 10.** Initial design matrix (continued)

| 1 | 2 | 3 | 4 | 5 | 6 | 7 | 8 |
|---|---|---|---|---|---|---|---|
| 8787 | 1 | 6036 | 1 | 5 | 2.92 | 1.6 | 2356 |
| 8787 | 1 | 6863 | 1 | 5 | 3.13 | 1.8 | 2356 |
| 8787 | 1 | 7730 | 1 | 5 | 3.34 | 2.0 | 2356 |
| 8787 | 1 | 8492 | 1 | 5 | 3.45 | 2.2 | 2356 |
| 8787 | 1 | 9107 | 1 | 5 | 3.62 | 2.4 | 2356 |
| 8787 | 1 | 9465 | 1 | 5 | 3.75 | 2.6 | 2356 |
| 8787 | 1 | 10166 | 1 | 5 | 3.90 | 2.8 | 2356 |
| 8787 | 1 | 11200 | 1 | 5 | 4.10 | 3.0 | 2356 |
| 8787 | 1 | 11395 | 1 | 5 | 4.21 | 3.2 | 2356 |

(b) The normalized decision matrix is as follows (Table 11).

**Table 11.** Normalized design matrix

| 1 | 2 | 3 | 4 | 5 | 6 | 7 | 8 |
|---|---|---|---|---|---|---|---|
| 0.58 | 0.58 | 0.22 | 0.58 | 0.58 | 0.26 | 0.21 | 0.58 |
| 0.58 | 0.58 | 0.25 | 0.58 | 0.58 | 0.28 | 0.24 | 0.58 |
| 0.58 | 0.58 | 0.28 | 0.58 | 0.58 | 0.30 | 0.27 | 0.58 |
| 0.58 | 0.58 | 0.30 | 0.58 | 0.58 | 0.31 | 0.29 | 0.58 |
| 0.58 | 0.58 | 0.33 | 0.58 | 0.58 | 0.33 | 0.32 | 0.58 |
| 0.58 | 0.58 | 0.34 | 0.58 | 0.58 | 0.34 | 0.35 | 0.58 |
| 0.58 | 0.58 | 0.37 | 0.58 | 0.58 | 0.35 | 0.38 | 0.58 |
| 0.58 | 0.58 | 0.40 | 0.58 | 0.58 | 0.37 | 0.40 | 0.58 |
| 0.58 | 0.58 | 0.41 | 0.58 | 0.58 | 0.38 | 0.43 | 0.58 |

(c) The average normalized weight matrix is given in Table 8

(d) And the weighted normalized matrix is obtained is given as Table 12

**Table 12.** Weighted normalized design matrix

| 1 | 2 | 3 | 4 | 5 | 6 | 7 | 8 |
|---|---|---|---|---|---|---|---|
| 0.38 | 0.38 | 0.20 | 0.53 | 0.58 | 0.26 | 0.17 | 0.43 |
| 0.38 | 0.38 | 0.23 | 0.53 | 0.58 | 0.28 | 0.20 | 0.43 |
| 0.38 | 0.38 | 0.25 | 0.53 | 0.58 | 0.30 | 0.22 | 0.43 |
| 0.38 | 0.38 | 0.27 | 0.53 | 0.58 | 0.31 | 0.24 | 0.43 |
| 0.38 | 0.38 | 0.30 | 0.53 | 0.58 | 0.33 | 0.27 | 0.43 |
| 0.38 | 0.38 | 0.31 | 0.53 | 0.58 | 0.34 | 0.29 | 0.43 |
| 0.38 | 0.38 | 0.34 | 0.53 | 0.58 | 0.35 | 0.32 | 0.43 |
| 0.38 | 0.38 | 0.36 | 0.53 | 0.58 | 0.37 | 0.33 | 0.43 |
| 0.38 | 0.38 | 0.37 | 0.53 | 0.58 | 0.38 | 0.36 | 0.43 |

(f) The positive and negative ideal solution (PIS and NIS) as given in Table 13.

**Table 13.** PIS and NIS matrix

| 1 | 2 | 3 | 4 | 5 | 6 | 7 | 8 |
|---|---|---|---|---|---|---|---|
| 0.38 | 0.38 | 0.20 | 0.53 | 0.58 | 0.26 | 0.36 | 0.43 |
| 0.38 | 0.38 | 0.37 | 0.53 | 0.58 | 0.38 | 0.17 | 0.43 |

After evaluating the decision matrix using TOPIS method, design index four was found to be best option (0.69). The selected index has reserve strength ratio of 2.2 with mass of 398 Ton. The RSR value is found to be well above the minimum prescribed value of 1.58 and 1.85 as per API and ISO studies respectively.

## 4. Conclusion

The study provides a multi criteria based decision making methodology for design of offshore structures. This methodology not only considers technical feasibility, but social and economic factors for selection of optimal design. The optimal design provides technically safe and sustainable design. Further, this methodology can be extended to design of floating structures for deep water also. A sensitivity study can also be performed for change is water depth and environmental conditions.

**Author Contributions:**

The first author Mr. Vishnu Murali (Ph.D. scholar) has developed the methodology for design of offshore structures considering sustainability. His work includes scripting in MATLAB and FE analysis is USFOS. He has also integrated USFOS-MATLAB for seamless working of optimization methodology. The second author Prof. Surendran Sankunny has provided the necessary inspiration and motivation for the work. He has contributed significantly to the research work in detailed correction and providing technical support for numerical analysis.

**Conflict of Interest:**

No conflict of interest was reported by the authors.

**Acknowledgments:**

## References

[ 1 ] Chew K-H, Tai K, Ng EYK, Muskulus M. Analytical gradient-based optimization of offshore wind turbine substructures under fatigue and extreme loads. Mar Struct. 2016, 47, 23–41.

[ 2 ] Gentils T, Wang L, Kolios A. Integrated structural optimisation of offshore wind turbine support structures based on finite element analysis and genetic algorithm. Appl Energy. Elsevier Ltd; 2017, 199, 187–204. Available from: http://dx.doi.org/10.1016/j.apenergy.2017.05.009.

[ 3 ] Gomes HM. Truss optimization with dynamic constraints using a particle swarm algorithm. Expert Syst Appl. Elsevier Ltd; 2011;38(1):957–68. Available from: http://dx.doi.org/10.1016/j.eswa.2010.07.086.

[ 4 ] Coello C a C, Pulido GT, Lechuga MS. Handling multiple objectives with particle swarm optimization. Evol Comput IEEE Trans. 2004, 8(3), 256–79.

[ 5 ] API. Recommended Practice for Planning, Designing and Constructing Fixed Offshore Platforms — Working Stress Design. Api Recomm Pract [Internet]. 2007, 24–WSD, 242.

[ 6 ] International Organization for Standards (ISO). Petroleum and natural gas industries — Fixed steel offshore structures. Iso 19902. 2007, 2007, 638.

[ 7 ] Nizamani Z. Environmental Load Factors and System Strength Evaluation of Offshore Jacket Platforms. 2015, 128.

[ 8 ] Potty NS, Sohaimi AFA. Ultimate Strength Assessment For Fixed Steel Offshore Platform. Malaysian J Civ Eng. 2013, 25(2), 128–53.

[ 9 ] Yukio U, Rashed SMH. The idealized structural unit method and its application to deep girder structures. Comput Struct. 1984, 18(2), 277–93.

[10] SINTEF GROUP. USFOS Getting Started. 2001, 106. Available from: www.usfos.com.

[11] Carbon Trust. Offshore wind power : big challenge, big opportunity Maximising the environmental, economic and security benefits Table of Contents. Renew Energy. 2009.

[12] Lozano-Minguez E, Kolios AJ, Brennan FP. Multi-criteria assessment of offshore wind turbine support structures. Renew Energy [Internet]. Elsevier Ltd; 2011, 36(11), 2831–7. Available from: http://dx.doi.org/10.1016/j.renene.2011.04.020.

[13] Vorpahl F, Popko W, Kaufer D. Description of a basic model of the "UpWind reference jacket" for code comparison in the OC4 project under IEA Wind Annex XXX. Fraunhofer Inst Wind. 2011, 1(February), 1–14.

[14] Montes-Iturrizaga R, Heredia-Zavoni E, Vargas-Rodríguez F, Faber MH, Straub D, de Dios de la O J. Risk Based Structural Integrity Management of Marine Platforms Using Bayesian Probabilistic Nets. J Offshore Mech Arct Eng . 2009, 131(1), 11602.

[15] Abdel Raheem SE. Nonlinear behaviour of steel fixed offshore platform under environmental loads. Ships Offshore Struct. Taylor & Francis; 2016, 11(1), 1–15. Available from: http://dx.doi.org/10.1080/17445302.2014.954301.

[16] Wei K, Myers AT. Directional effects on the reliability of non- axisymmetric support structures for offshore wind turbines under extreme wind and wave loadings. Eng Struct. Elsevier Ltd; 2016, 106:68–79. Available from: http://dx.doi.org/10.1016/j.engstruct.2015.10.016.

[17] Kennedy J, Eberhart R. Particle Swarm Optimization. 1995,1942–8.

[18] Perez RE, Behdinan K. Particle swarm approach for structural design optimization. Comput Struct. 2007, 85(19–20), 1579–88.